ADVANCED ELECTRONIC MATERIALS
www.advelectronicmat.de

Recent Advances in Understanding the Structure and Properties of Amorphous Oxide Semiconductors

Julia E. Medvedeva, D. Bruce Buchholz, and Robert P. H. Chang*

In memory of Arthur J. Freeman, a great advisor, mentor, and colleague

Amorphous oxide semiconductors (AOSs)—ternary or quaternary oxides of post-transition metals such as In-Sn-O, Zn-Sn-O, or In-Ga-Zn-O—have been known for a decade and have attracted a great deal of attention as they possess several technological advantages, including low-temperature large-area deposition, mechanical flexibility, smooth surfaces, and high carrier mobility that is an order of magnitude larger than that of amorphous silicon (a-Si:H). Compared to their crystalline counterparts, the structure of AOSs is extremely sensitive to deposition conditions, stoichiometry, and composition, giving rise to a wide range of tunable optical and electrical properties. The large parameter space and the resulting complex deposition–structure–property relationships in AOSs make the currently available theoretical and experimental research data rather scattered and the design of new materials difficult. In this work, the key properties of several In-based AOSs are studied as a function of cooling rates, oxygen stoichiometry, cation composition, or lattice strain. Based on a thorough comparison of the results of ab initio modeling, comprehensive structural analysis, accurate property calculations, and systematic experimental measurements, a four-dimensional parameter space for AOSs is derived, serving as a solid foundation for property optimization in known AOSs and for design of next-generation transparent amorphous semiconductors.

1. Introduction

The research area of transparent conducting oxides (TCOs) dates back to 1907 when CdO was reported to combine both optical transparency in the visible range and good electrical conductivity.[1] Following the discovery of SnO_2 with a similar unique combination of properties,[2] several patents were filed in the 1940s to employ TCOs as antistatic coatings and transparent heaters—long before the discovery of the now well-known Sn-doped In_2O_3 (ITO) and Al-doped ZnO,[3] widely employed as flat panel display electrodes in the past decades. Despite great technological demand for TCOs[4–20] and extensive experimental efforts to improve the conductivity via impurity doping,[21,22] to tune the work function and carrier concentration via cation composition,[23–28] to achieve two-dimensional transport via heterointerfaces,[29] and to p-dope the oxides toward active layers of transparent electronics,[30–32] theoretical understanding of these fascinating materials has lagged behind significantly. The first electronic band structure of ITO was calculated in 2001;[33] the role of native defects in prototype TCOs was understood after 2002;[34–37] the properties of multi-cation TCOs were first considered in 2004[37–42] followed by modeling of novel TCO hosts[43,44] and spin-dependent transport in transition-metal-doped TCOs;[45] the nature of the band gap in In_2O_3 was clarified in 2008;[46] and a first high-throughput search for p-type TCOs was performed in 2013.[47]

Complex oxides that consist of multiple post-transition metals, such as $InGaZnO_4$, have recently become competitive with silicon as the active transistor layer to drive arrays of pixels in large area displays.[9,13–19,24] As the billion-dollar display industry moves forward, the amorphous phase of the complex oxides is favored both for flexible and high-resolution display applications.[13–16,48–59] The unique properties of AOSs were first demonstrated in 1990,[60] and the research area has been growing exponentially since then. Unlike Si-based semiconductors, AOSs were shown to exhibit optical, electrical, thermal, and mechanical properties that are comparable or even superior to those possessed by their crystalline counterparts.[48–58] **Table 1** summarizes the key physical properties of best-performing crystalline TCOs and AOSs; the differences (or the lack thereof) between the two will be discussed in detail in the respective sections below.

Many fundamental aspects of AOSs have been addressed theoretically. The first molecular dynamics (MD) simulations

Prof. J. E. Medvedeva
Department of Physics
Missouri University of Science and Technology
1315 N Pine Street, Rolla 65409, USA
E-mail: juliaem@mst.edu

Dr. D. B. Buchholz, Prof. R. P. H. Chang
Materials Science and Engineering Department
Northwestern University
2220 Campus Drive, Evanston, IL 60208, USA

© 2017 The Authors. Published by WILEY-VCH Verlag GmbH & Co. KGaA, Weinheim. This is an open access article under the terms of the Creative Commons Attribution-NonCommercial-NoDerivs License, which permits use and distribution in any medium, provided the original work is properly cited, the use is non-commercial and no modifications or adaptations are made.

DOI: 10.1002/aelm.201700082

Table 1. Basic properties of crystalline TCOs and transparent amorphous oxide semiconductors.

Property	Crystalline Transparent Conducting Oxides	Amorphous Oxide Semiconductors
Structural	Ordered network of regular MO polyhedra	Disordered network of distorted MO_x
Optical	Optical band gap >3eV	Tail states, reduced optical band gap
	Transparency in the visible 80–90%	Transparent upon Burstein–Moss shift
Electrical:		
– Carrier concentration	$n = 10^{19}$ cm^{-3} (V_O); $n = 10^{21}$ cm^{-3} (doping)	$n< = 10^{20}$ cm^{-3} (non-stoichiometry)
– Carrier mobility	$\mu = 10$–100 cm^2 V^{-1} s^{-1}	$\mu = 10$–60 cm^2 V^{-1} s^{-1}
Thermal	Few stable compositions, $\kappa = 1$ W mK^{-1}	Wide range of stable compositions, $\kappa = 1$ W mK^{-1}
Mechanical	Brittle	Bendable

of amorphous indium oxide appeared in 2009,[61] followed by models of electron transport in multi-cation AOSs,[62–67] DFT calculations of defect formation,[68–75] and statistical descriptions of amorphous network.[76–78] However, several key questions regarding the nanostructure and morphology, crystallization, carrier generation, and conductivity mechanisms in AOSs remain unanswered and require a unified theoretical framework capable of handling all these aspects in tandem.

Tunable electrical conductivity—the ability to change carrier concentration over a wide range of useful values while maintaining superior mobility—is arguably the central technological advantage of an AOS.[50,62,64,65,79–83] In marked contrast to the crystalline TCOs, where the electron mobility is governed primarily by the scattering on ionized impurities, phonons, and grain boundaries, the charge transport in AOSs is more complex. Although amorphous materials lack grain boundaries, the structural long-range disorder, as well as strong local distortions in the metal–oxygen (M–O) polyhedra, give rise to several new terms in the electron transport. Adhering to the Drude model, the electron mobility in an AOS can be represented with the following equation:

$$\frac{1}{\mu} = \frac{m^*}{e}\left(\frac{1}{\tau_{\text{crystallinity}}} + \frac{1}{\tau_{\text{composition}}} + \frac{1}{\tau_{\text{defects}}} + \frac{1}{\tau_{\text{vibrons}}} + \frac{1}{\tau_{\text{strain}}}\right) \quad (1)$$

where the contributions to the overall relaxation time are due to i) size and density of nanocrystalline inclusions; ii) spatial distribution and clustering of incorporated cations; iii) local point defects; iv) thermal vibrations; and v) piezoelectric effects associated with internal lattice strain. Clearly, the above classifications are figurative; the terms are likely to be intermixed for most AOS materials. For example, cation composition has a strong effect on the crystallization processes, defect formation, thermal properties, and can introduce significant lattice strain in amorphous structure. However, understanding the microscopic origins for each of the above terms via systematic investigations will help untangle the different contributions to the complex transport phenomena in AOSs.

Julia E. Medvedeva is a professor of physics and a senior investigator at Materials Research Center of Missouri University of Science and Technology. She received her Ph.D. from the Russian Academy of Science in 2002 and worked as a pre- and post-doctoral fellow at Northwestern University in Arthur J. Freeman's group. Her expertise is in first-principles density functional calculations of the structural, electronic, optical, and mechanical properties of a wide range of materials, including metal oxides and nitrides, alloys, and strongly correlated materials.

D. Bruce Buchholz is the manager of the Pulsed Laser Deposition Facility at Northwestern University. He received a B.S. in chemical engineering from the University of Illinois at Urbana in 1977, a M.S. in chemistry from Northwestern in 1983, and a Ph.D. in Materials Science from Northwestern in 1997. He worked at Western Electric as a thin film engineer from 1977, then at the Technology Transfer Department to introduce new thin-film processes from Bell Labs to Western Electric, and then at a prototype center in Bell Labs. Since 2001 he has worked at Northwestern.

R. P. H. (Bob) Chang's current research interests include amorphous semiconducting films, nanostructured materials, nanophotonics, and advanced solar cell development. Chang served as the President of the Materials Research Society in 1989. He is the General Secretary and Founding President of the International Union of Materials Research Societies (IUMRS). He led the first NSF national nanotechnology education center for K-graduate level students. He was honored in 2005 with the NSF Director's Distinguished Teaching Scholar Award for his contributions to materials research and education. Chang is a Fellow of the American Vacuum Society and the Materials Research Society.

 © 2017 The Authors. Published by WILEY-VCH Verlag GmbH & Co. KGaA, Weinheim

Accurate determination of the structural characteristics of an AOS remains challenging. Whereas Si or Ge-based semiconductors or glasses like SiO_2 from the main group metal oxides are covalent, the oxides of post-transition metals possess weaker metal–oxygen bonding, primarily ionic in nature. The strength of the M–O bonding determines the clarity of the local polyhedral structure. Strong local distortions in the M–O polyhedra in AOSs are not expected to affect the electron effective mass or the band gap—both should remain similar to the values in the corresponding crystalline counterparts.[39] On the other hand, the local distortions may affect the medium-range structure (e.g., edge or corner-sharing between the M–O polyhedra and their integration into an extended network) and facilitate the formation of structural defects that govern the degree of electron localization near the valence and conduction band edges and deep inside the band gap. Hence, instead of classical atomistic approaches commonly employed for modeling of glasses, quantum-mechanical molecular dynamics simulations combined with accurate density-functional calculations are required for AOSs in order to reliably describe the formation of both shallow and deep defects responsible for carrier generation and the charge transport limited by electron scattering and trapping. In addition, accurate characterization of the structural features beyond the first shell (i.e., beyond the nearest neighbors) is necessary in order to explain the high sensitivity of the AOSs properties to the deposition[84] and post-deposition conditions,[64] particularly oxygen environment,[85] as well as the chemical composition of the sample.[67,86]

In this work, ab initio MD simulations and hybrid-functional DFT-based electronic structure calculations are performed i) to systematically study the local and medium-range structural characteristics of several prototype In-based oxides with different degree of amorphization, oxygen stoichiometry, cation composition, and/or lattice strain and ii) to connect the structural peculiarities to the resulting electronic, optical, or thermal properties of each material. Based on good agreement between the theoretically established trends and those observed experimentally, a unified model for prototype In-based AOS is proposed. The derived set of generic growth-structure-property relationships will help expedite the search for optimal preparation conditions—or those that ensure a desired set of properties—within the large parameter space of AOSs.

2. Key Structural Properties of Amorphous Indium Oxide

Theoretically, the atomic structure of an amorphous material can be obtained using molecular dynamics (MD) simulations. In a liquid-quench approach, an initial crystalline structure is melted at a temperature well above the oxide melting point to remove the crystal structure memory and then rapidly quenched to a low temperature, usually to 100 K or below. Prior to optimization of the atomic coordinates within density functional theory (DFT) at 0 K, the quenched structure is equilibrated at room temperature to ensure that an energetically stable solution is reached. The electronic properties are then calculated for the DFT-optimized structure using local density approximation, generalized gradient approximation, or a hybrid functional approach for a more accurate description of the occupied and empty states.

Our analysis begins from a prototype AOS structure—undoped stoichiometric indium oxide. **Figure 1** illustrates the pair correlation functions (PCFs) of 1) indium oxide melted at

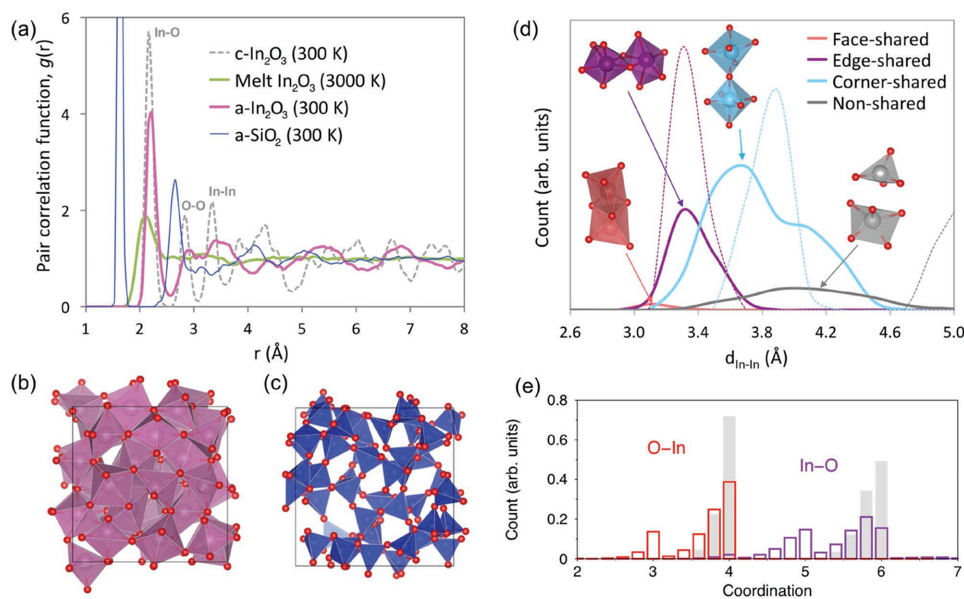

Figure 1. Structural properties of amorphous indium oxide as obtained from ab initio MD simulations. a) The calculated pair correlation function for In_2O_3 melt (green); amorphous In_2O_3 (purple); amorphous SiO_2 (blue); and crystalline In_2O_3 (dashed grey line). b) The atomic structure of amorphous In_2O_3. Oxygen or indium atoms are represented as small red or large purple spheres, respectively. c) The atomic structure of amorphous SiO_2. Oxygen or silicon atoms are represented as small red or large blue spheres, respectively. d) Distribution of the face, edge, corner, and non-shared In neighbors as a function of the In-In distance in amorphous (solid lines) and crystalline (dashed line) In_2O_3. e) Distribution of differently coordinated In and O atoms in amorphous In_2O_3.

© 2017 The Authors. Published by WILEY-VCH Verlag GmbH & Co. KGaA, Weinheim

3000 K for 30 ps, 2) amorphous indium oxide quenched from the melt down to 100 K at a rate of 200 K/ps and then equilibrated at 300 K for 6 ps, and 3) crystalline In_2O_3 structure held at room temperature for 6 ps. In the amorphous state, only the first-shell peak that corresponds to the nearest In–O bonds, is clearly defined; at a longer range, all structural features are suppressed (Figure 1a). The latter highlights an important difference between an amorphous oxide semiconductor and a glass; for example, amorphous SiO_2. As one can see from the atomic structure of amorphous SiO_2 obtained using MD simulations with the same quench rates as for the amorphous indium oxide, Figure 1b and 1c, the tetrahedral coordination of Si is preserved in the glass phase—as signified by the narrow Si–O peak and a well-defined O–O peak in the distribution function. The first-shell metal–oxygen structure, that is, the Si–O distances, Si–O coordination, and O–Si–O angles, inside the polyhedra closely correspond to those of the crystalline oxide. In marked contrast to a random arrangement of the regular SiO_4 polyhedra, amorphous indium oxide features highly distorted InO_x polyhedra: the O–O peak in PCF is suppressed (Figure 1a) and the average variance of the In–O distances at room temperature is 8.4×10^{-3} Å^2—an order of magnitude larger than that in amorphous SiO_2, 8.5×10^{-4} Å^2. The large distortions in the local structure in the amorphous semiconductor originate from the weak, ionic bonding between oxygen atoms and the spherically symmetric s-orbitals of the post-transition metal. As a result, the average In–O coordination is reduced from 6.0 to 5.3 upon the crystalline-to-amorphous transition, and over 25% of the In atoms have a coordination of five or below (Figure 1e)—even in the perfectly stoichiometric case, that is, for the O/In ratio of 1.50.

Combining the irregular InO polyhedra into a network determines the medium-range In–In structure. In bixbyite In_2O_3, the second and third shells of indium are associated with six In neighbors at 3.3 Å that share two oxygen atoms with the central In atom (i.e., the corresponding polyhedra are edge-shared) and six In neighbors at 3.8 Å that share one oxygen atom (corner-shared polyhedra), respectively. In the amorphous phase, a significant number of edge-shared connections become corner-shared (Figure 1d): out of the total number of all In–In pairs that share one, two, or three oxygen atoms, as much as 80% share only a single oxygen atom. The In–O–In angles for the corner-sharing connections vary from 95° to 160° (with the peak located at 115°). The corresponding distance distribution is nearly twice as wide as the corner-sharing distribution in the crystalline In_2O_3 and overlaps significantly with the distance distribution for the edge-shared In–In pairs (Figure 1d). Consequently, the two peaks in the In–In distribution are nearly indistinguishable and hard to resolve experimentally (i.e., the coordination number and Debye–Waller factor for the second and third shells cannot be uniquely fit). Yet, information regarding the In–In shells is essential for understanding the properties of AOSs: it has been shown that medium-range ordering plays a crucial role in the carrier transport of amorphous indium oxide[84] as discussed in the next section.

Another important structural peculiarity of the AOSs is the existence of non-shared InO polyhedra. In perfectly stoichiometric amorphous indium oxide, there is an appreciable number of the In–In pairs that do not share an oxygen atom although the two are located at a short distance from each other, namely 3.4 – 4.6 Å (Figure 1d). As it will be shown below, the presence of such non-shared and often under-coordinate In atoms (and, similarly, the under-coordinate oxygen atoms; c.f., Figure 1e) leads to the formation of tail states near the oxide band edges.[87] These defect states may contribute to the optical absorption in the visible range (resulting in a negative bias illumination stress instability in AOS-based thin film transistors[88]) and limit carrier transport in AOSs.

3. Properties of Indium Oxide across Crystalline to Amorphous Transition

Upon transition from crystalline to amorphous phase, the structure of undoped indium oxide grown by pulsed laser deposition (PLD) using different substrate temperatures, T_d, changes from 1) crystalline grains, T_d = 600 °C, to 2) a multiphase mixture with the crystalline fraction decreasing linearly from 0.82 at T_d = 200 °C to 0.36 at T_d = 25 °C, and to 3) an amorphous material with no X-ray Bragg peaks below T_d = 0 °C.[84] Accordingly, the transport regimes across the transition may be classified as band conductivity limited by grain boundaries (Hall mobility μ = 70 cm^2 V^{-1} s^{-1} for T_d > 400 °C); multiphase scattering/percolation (μ = 20–40 cm^2 V^{-1} s^{-1} for T_d = 50–300 °C); and electron localization in the amorphous phase (μ = 20 cm^2 V^{-1} s^{-1} for T_d < –50 °C). Strikingly, however, when the crystalline fraction of In_2O_3 drops to zero at T_d = 0 °C, the Hall carrier mobility reaches as much as 60 cm^2 V^{-1} s^{-1}, nearly the value measured in undoped crystalline In_2O_3.[84] Scattering alone cannot explain the observed mobility peak because: i) the size of nano-crystalline In_2O_3 inclusions observed by high-resolution transmission electron microscopy (HR-TEM) decreases smoothly across the transition, from 2.2–3.4 nm at T_d = 0 °C to 2.0–2.4 nm at T_d = –50 °C,[84] and ii) the carrier concentration remains nearly constant, $n = 2.7 - 3.2 \times 10^{20}$ cm^{-3} (in samples grown with oxygen partial pressure of 8 mTorr[84]) for the deposition temperatures from –50 °C to +100 °C. Moreover, the average metal–oxygen and metal–metal distances vary insignificantly (< 2%) upon the crystalline-amorphous transition and cannot explain the mobility changes.[84]

A thorough systematic comparison of the local structural characteristics of the amorphous indium oxide obtained from extended X-ray absorption fine structure (EXAFS) measurements and from ab initio MD liquid-quench simulations has shown that the major differences occur in the second and third indium shells,[84] with the number of the edge-sharing InO polyhedra being greatly diminished in the amorphous phase; c.f., Figure 1d. The local structure evolved as a function of deposition temperature in the case of the films analyzed by EXAFS and as a function of quench rate in the case of MD simulations. A striking agreement was observed between the structural trends observed by EXAFS as a function of deposition temperature and the structural trends observed for MD simulations as a function of quench rate. Based on the excellent agreement between the measured and simulated structures, the experimental deposition temperature scale (T_d = 25 °C to –100 °C) was aligned with the MD quench rate scale (5–700 K ps^{-1}).[84] Further look into the theoretical atomistic structures

© 2017 The Authors. Published by WILEY-VCH Verlag GmbH & Co. KGaA, Weinheim

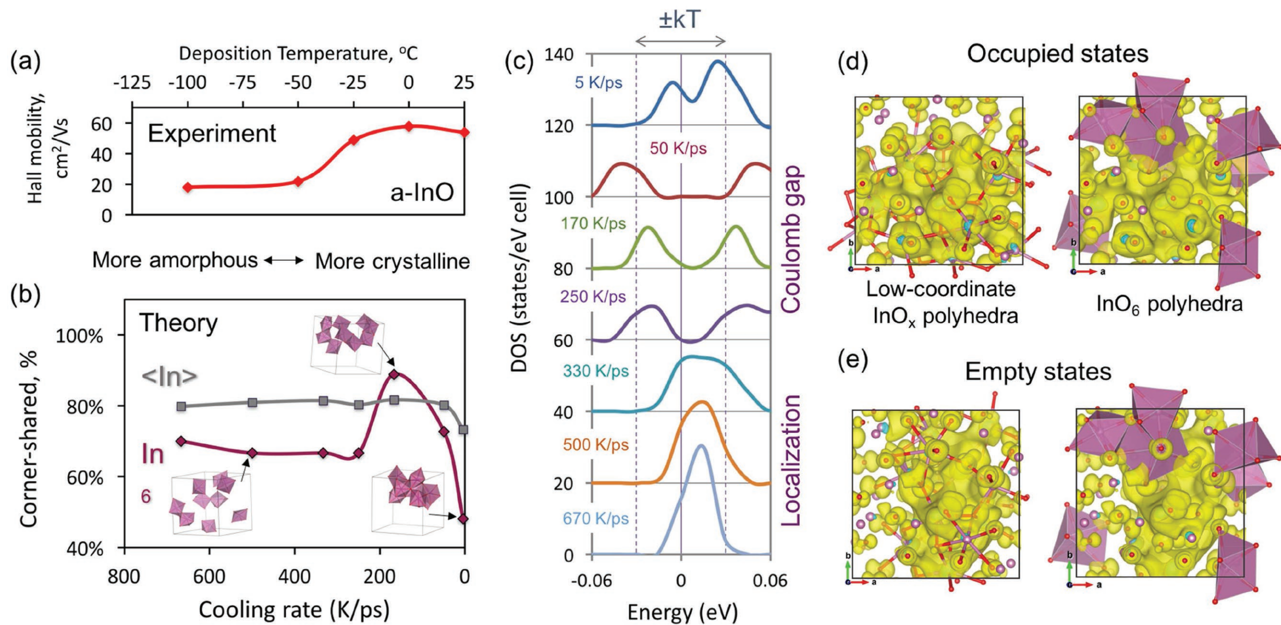

Figure 2. Structural and electronic properties of amorphous indium oxide with different degree of amorphization. a) Experimental Hall mobility as a function of deposition temperature in amorphous indium oxide grown using pulsed laser deposition under oxygen partial pressure of 8 mTorr. b) Fraction of corner-shared InO–InO or InO_6–InO_6 polyhedra out of the total number of the In–In pairs that share one, two, or three oxygen atoms in amorphous indium oxide structures obtained with different MD quench rates. Spatial distribution of the InO_6 polyhedra in the supercell ranges from clusters (slow cooling), to corner-shared chains (intermediate cooling); to random distribution (fast cooling). c) The calculated density of states near the Fermi level in amorphous indium oxide structures obtained with different MD quench rates. d) The charge density distribution calculated for occupied and e) empty states near the Fermi level for the amorphous structure obtained with 170 K ps^{-1} quench rate.

obtained at different quench rates reveals that the spatial distribution of the indium atoms with octahedral coordination; that is, the six-fold coordination with oxygen atoms, varies from 1) clusters of InO_6 polyhedra with short-distant edge-sharing fraction reaching 50% (same as in crystalline In_2O_3) in the amorphous structures obtained using slow quench rates, to 2) chains of InO_6 polyhedra primarily connected via long-distant corner-sharing in structures quenched with intermediate rates, and to 3) a random distribution of disconnected InO_6 polyhedra in the most amorphous structures (quench rates 400 K ps^{-1} and above; **Figure 2**). Although slower cooling rates (K ns^{-1}) would be required to describe the crystallization process ($T_d > 50$ °C), ab initio MD simulations are able to capture the important structural variations that occur during the transition into the amorphous state. We believe that the clustering of the InO_6 polyhedra found in the amorphous structures upon slow quenching (Figure 2b), corresponds to the initial nucleation of the In_2O_3 nanocrystallites that have been observed using HR-TEM.[84] As the deposition temperature changes from $T_d = 0$ °C to $T_d = 150$ °C, the size of the nanocrystallites increases and the scattering-limited mobility decreases from 60 cm^2 V^{-1} s^{-1} to 20 cm^2 V^{-1} s^{-1}, respectively. When the crystalline fraction exceeds 80% ($T_d > 200$ °C), the carrier mobility begins to increase toward the value of the crystal.

Thus, the three-fold increase in the mobility (in samples deposited at $T_d = 0$ °C) is attributed to the formation of corner-shared InO_6 polyhedra chains (in structures obtained at MD quench rate of 200 K ps^{-1}). Accurate density-functional electronic band structure calculations of the oxides with different degree of amorphization (cooling rates 5 – 700 K ps^{-1}) help determine the conductivity mechanisms below the crystalline-amorphous transition. The calculated density of states (DOS) for the structures obtained with the rates of 50 – 250 K ps^{-1} features two peaks with a clear gap at the Fermi level (Figure 2c). The gap, known as a Coulomb gap,[89] separates the occupied and empty states and signifies that the electron–electron interactions (a Coulomb blockade) result in the electron localization in a particular state below the Fermi level, while the empty state above E_F is available for the electron to hop through—once the temperature is high enough. The charge density distribution calculated for the energy ranges that correspond to the two states, clearly illustrates that the electron is localized along a chain in a particular direction, whereas the empty, conduction path runs in a different (perpendicular) direction. Importantly, both chains are formed by low-coordinate under-shared InO polyhedra, and in both cases the charge avoids the indium atoms with octahedral coordination, that is, those that reach their natural coordination of 6 (Figure 2d and e). This suggests that the long-range formation of the connected InO_6 polyhedra leads to oxygen depletion in the areas adjacent to the chains and the charge is localized in the oxygen-depleted regions.

Above and below the mobility maximum, that is, for slower (5 K ps^{-1}) or faster-quenched (300 K ps^{-1}) amorphous structures, the Coulomb gap softens as the two states overlap resulting in a nonzero DOS (Figure 2c). This occurs due to a weaker electron repulsion caused by structural reorganization: the long-range structural correlations, that is, the InO_6 chains, are suppressed by the increased disorder below the mobility peak, whereas above the peak, the additional energy (higher T_d) leads to the formation of short-distant edge-shared InO_6

© 2017 The Authors. Published by WILEY-VCH Verlag GmbH & Co. KGaA, Weinheim

clusters. Finally, in the structures obtained with the quench rates above 500 K ps^{-1}, the two-state structure completely disappears and a single localized state is formed in the DOS—as should be expected for the most disordered structures.

Two important points must be made here. First, we stress that the specific direction of the InO_6 chain in our calculations does not carry any meaning and is pertinent to the particular realization. MD simulations under identical conditions (quench rates) or with a larger/smaller supercell (while keeping the same O/M ratio) were found to result to different atomic configuration; nonetheless, the outcome properties—a chain of InO_6 polyhedra in the structure and a Coulomb gap in the density of states—were preserved in each case. In a real sample of indium oxide, multiple InO_6 chains of various lengths and orientations are expected to coexist, all contributing to overall enhancement of the carrier mobility.

Second, the medium-range structural correlations in amorphous oxides are likely to be highly sensitive to deposition and post-deposition conditions (temperature, time, and ambient), film thickness, as well as to cation composition since all the above may have a strong effect on the In coordination and the spatial distribution of the differently coordinated InO polyhedra. In the next sections, the results of thorough theoretical investigations are shown to provide important insights into the role of oxygen content (Section 5), cation composition (Section 6), and lattice strain (Section 7) on the local and medium-range structure of AOSs.

Here, we give an example of how film thickness affects the mobility behavior. In 350–450 nm and 850–1050 nm thick films of $(ZnO)_{0.15}$ $(In_2O_3)_{0.70}$ $(SnO_2)_{0.15}$ (or ZITO) grown by PLD at an oxygen partial pressure of 8 mTorr, the measured Hall mobility reaches the maximum value of 50 cm^2 V^{-1} s^{-1} at the deposition temperature of T_d = 150 °C, at which both oxide films are X-ray amorphous. However, the shape of the $\mu(T_d)$ curve differs between the two films. In the thinner film, the mobility drops to 35 cm^2 V^{-1} s^{-1} at T_d = 100 °C and to 20 cm^2 V^{-1} s^{-1} at T_d = 300 °C, illustrating that the multi-cation composition broadens the $\mu(T_d)$ curve as compared to the sharp mobility peak in amorphous indium oxide (see Supporting Information; the role of cation composition in ternary In-based oxides is discussed in more detail in Section 6). In the thicker film, the mobility dependence on the deposition temperature is even weaker: the mobility is equal to 30–32 cm^2 V^{-1} s^{-1} at T_d = –25 °C and at T_d = 300 °C and it nearly plateaus above and below the peak value, namely from 100 °C to 200 °C (see Supporting Information). Clearly, the film thickness affects the formation and/or distribution of the InO_6 chains, opening up a possibility to tune the mobility behavior of AOSs for a specific technological application.

4. Carrier Generation and Defect Formation in AOSs

The key features of the electronic band structure of a transparent conducting oxide host—a wide optical band gap and a single highly-dispersed conduction band—originate from the metal–oxygen interactions.[90] Since the local structure; that is, the M–O distances and coordination, remains nearly intact upon amorphization,[84] the band gap and the electron effective mass of an AOS should deviate insignificantly from the corresponding crystalline values. Indeed, in the stoichiometric amorphous indium oxide, a-$In_2O_{3.00}$, the delocalized nature of the conduction band formed from the M-*s*–O-*p* states is preserved under the structural transition, **Figure 3**, so that the calculated supercell electron effective mass, 0.20 m_e, is nearly identical to that in the crystalline In_2O_3, 0.22 m_e. However, owing to the wide distribution of the In–O coordination numbers in the amorphous state (Figure 1e), the charge density distribution calculated for the empty conduction band is not uniform: a notable charge density accumulation is found in the interstitial area between several under-coordinate In atoms, Figure 3d–f: the charge originates at the In atom with the lowest coordination number (CN = 4.4), and spills toward its In neighbors that are also under-coordinated (CN = 4.8). Low coordination numbers imply that the corresponding InO polyhedra are likely to be under-shared—owing to the lack of oxygen atoms in the vicinity. In the cluster of the under-coordinate indium atoms, the shortest In–In distance (3.3 Å) corresponds to an edge-sharing connection as expected (c.f., Figure 1d), while the other two In–In pairs are under-shared: the In atoms located at 3.5 Å from each other, share a corner (although there are edge-shared In–In pairs at this distance; Figure 1d) and the In–In pair at 3.8 Å does not share an oxygen atom. The close proximity of several under-coordinate under-shared In atoms indicates the onset of the medium-range correlations discussed in the previous section, and the charge density redistribution in the empty conduction band of the stoichiometric amorphous indium oxide is in accord with the well-defined conduction paths shown in Figure 2d and e.

In contrast to the conduction states that remain delocalized in the stoichiometric amorphous indium oxide, the structural disorder reveals itself in the appearance of strongly localized states near the top of the valence band (Figure 3a). These tail states[73,75,87,91] originate from the charge localization at under-coordinate oxygen atoms (with a coordination number 3 or below; c.f., Figure 1e) and contribute to the optical absorption within the visible range, that is, at 2–3 eV (Figure 3c). The degree of localization and the energy location of the tail states with respect to the valence band edge depends strongly on the oxygen/metal ratio (as discussed in more details later in this section) and on the cation composition (see Section 5.4).

Similar to undoped TCOs, carriers in AOSs are introduced in materials grown under oxygen-reduced conditions. In amorphous indium oxide grown by PLD at T_d = –25 °C with the oxygen partial pressure varied from 1 mTorr to 16 mTorr during the deposition, the carrier concentration increases linearly with decreasing $p(O_2)$, achieving $n = 5 \times 10^{20}$ cm^{-3} (**Figure 4**). Ab initio MD simulations of non-stoichiometric indium oxide, a-$In_2O_{2.96}$, reveal a rigid-band-like shift of the Fermi level: the occupied states at the bottom of the conduction band and in the vicinity of the Fermi level remain delocalized—in accordance with the unchanged mobility for the samples grown with $p(O_2)$ = 8–16 mTorr, μ = 50 cm^2 V^{-1} s^{-1} (Figure 4a). The charge density distribution calculated for the partially occupied conduction band shows a weak electron localization in the area surrounded by under-shared In atoms (Figure 3e). Similar to the stoichiometric case, the charge originates at an under-coordinate

© 2017 The Authors. Published by WILEY-VCH Verlag GmbH & Co. KGaA, Weinheim

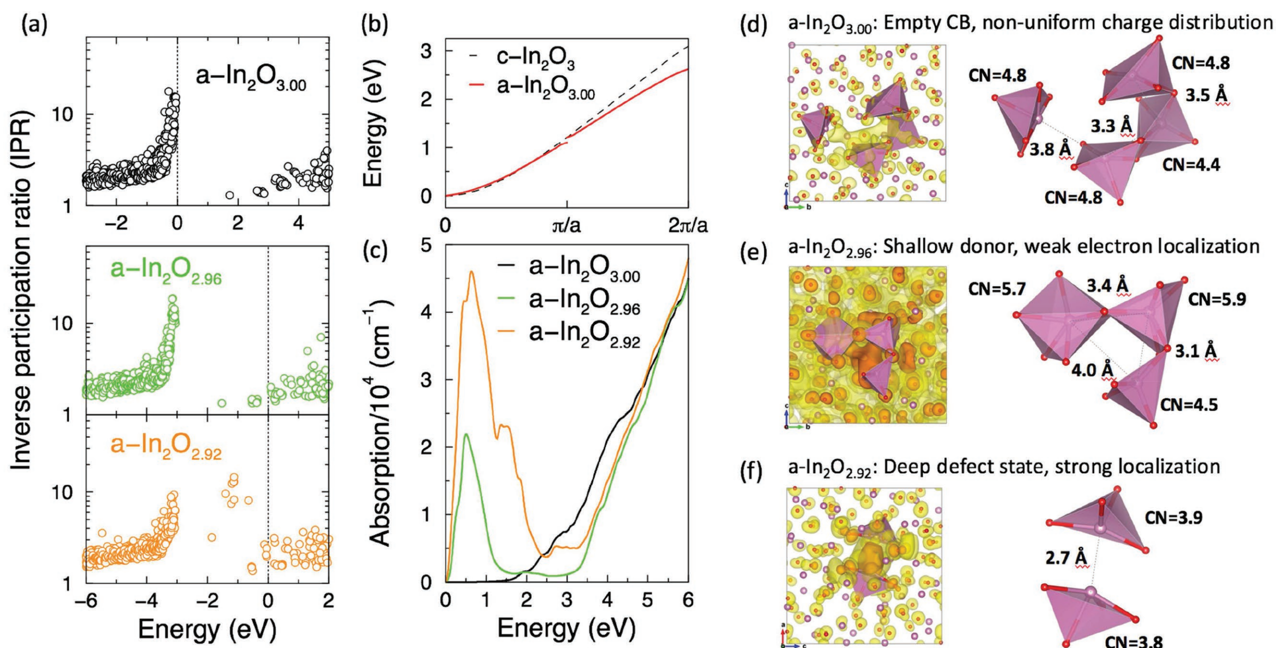

Figure 3. Electronic properties of amorphous indium oxide structures with different oxygen stoichiometry. The atomic structures were obtained using ab initio MD simulations with quench rate of 200 K ps^{-1} and optimized using DFT-PE approximation; the electronic structure was calculated using hybrid HSE functional. a) The calculated inverse participation ratio in a-$In_2O_{3-\delta}$ structures. The Fermi level is at 0 eV. b) The electronic band structure of the conduction band in crystalline (dashed line) and amorphous (solid red line) stoichiometric indium oxide. c) The calculated optical absorption in a-$In_2O_{3-\delta}$ structures. d–f) The charge density distribution calculated for the conduction band in stoichiometric and non-stoichiometric amorphous indium oxides.

In (the coordination number is 4.5) and spills toward two In neighbors located at 3.1 Å and 4.0 Å from the under-coordinate In atom. Such In–In distances correspond to face- and corner-sharing (c.f., Figure 1d); however, the respective In atoms share only two and no oxygen atoms, respectively. Structurally, the "void" between the three under-shared low-coordinate In atoms (Figure 3d and e) resembles an oxygen vacancy in a crystalline oxide where three or four metal atoms also lose sharing when the defect is introduced; a conceptual analogy with charged oxygen vacancy defects has also been suggested for amorphous oxides.[55] From the electronic structure point of view, however, we argue that the crystalline and amorphous oxides are fundamentally contradistinctive: owing to the many degrees of freedom of the amorphous structure and its ability to accommodate an oxygen "vacancy" by structural relaxation beyond the next-nearest neighbors, the under-shared In defect represents a shallow donor state in a-$In_2O_{2.96}$.

Upon the degenerate doping of the non-stoichiometric amorphous indium oxide, the optical band gap broadens (due to Burstein–Moss shift) and the material becomes transparent within the entire visible region (Figure 3c). Further decrease of the oxygen content in amorphous indium oxide leads to the formation of a strongly localized state in the band gap. For a-$In_2O_{2.92}$, a deep defect is formed at about 1.2 eV below the Fermi level (Figure 3a); the charge density distribution calculated for the defect state reveals that the strong localization occurs between two under-coordinate In atoms (the coordination numbers are 3.8 and 3.9) that do not share an oxygen atom between them—despite being located at a short distance of 2.7 Å (that is comparable to the metallic In–In distance in the elemental In crystal; Figure 3f). The strong electron localization between the under-coordinate under-shared In atoms in the oxygen-deficient amorphous oxides is expected to limit the carrier mobility due to charge scattering; indeed, the measured Hall mobility is suppressed to 10 $cm^2 V^{-1} s^{-1}$ at $p(O_2)$ = 1 mTorr (Figure 4a). In addition to the detrimental effect on the carrier transport, the deep defects contribute to optical absorption (Figure 3c), reducing the optical transmission within the visible range and being responsible for darker coloration of the AOSs samples.

The role of the [Oxygen]/[Metal] ratio in the formation of both the valence and conduction defect states is summarized in Figure 4b. In the perfectly stoichiometric case; that is, when [O]/[In] = 1.50 in the undoped indium oxide, most of the In atoms have high coordination with oxygen atoms and most of the InO polyhedra are shared according to the corresponding In-In distances, namely, edge-shared for $d_{In-In} \approx 3.4$ Å and corner-shared for $d_{In-In} \approx 3.7$ Å. All deviations in the coordination numbers or polyhedra sharing are absorbed by the amorphous structure via local polyhedral distortions and the MO network reorganization; as a result, the conduction band is empty. When the [O]/[M] ratio decreases below the stoichiometric value, the number of under-coordinate metal atoms increases; clustering of such under-coordinate In atoms into a group of under-shared polyhedra leads to the formation of an oxygen-depleted area that structurally is similar to the In–O features around an oxygen vacancy in the crystalline oxides. Electronically, the defect corresponds to a shallow electron donor and, in marked contrast to the crystalline oxides, exhibits very weak electron localization—owing to the ability of the amorphous

© 2017 The Authors. Published by WILEY-VCH Verlag GmbH & Co. KGaA, Weinheim

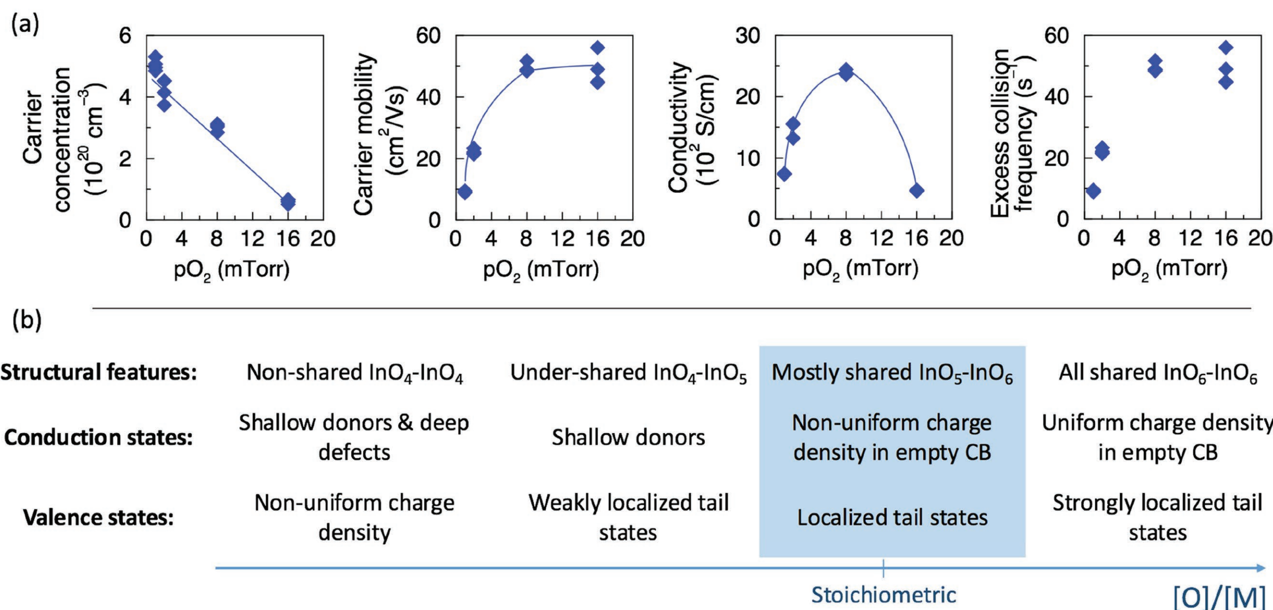

Figure 4. Electrical properties and defect formation in amorphous indium oxide. a) Experimental Hall mobility, carrier concentration, conductivity, and excess collision frequency (see Supporting Information) in amorphous indium oxide films of 270–390 nm thickness grown by PLD at deposition temperature $T_d = -25$ °C as a function of oxygen partial pressure. b) Summary of the structural peculiarities and the resulting electronic features near the valence and conduction band edges for AOSs as a function of variable [Oxygen]/[Metal] ratio.

structure to reduce the charge imbalance via a long-range structural relaxation around the defect. The theoretical predictions of weak electron scattering in marginally under-stoichiometric amorphous oxides are corroborated by our experimental observations of the constant carrier mobility for the samples grown with the O_2 pressures of 8–16 mTorr as well as the low excess collision frequency (see Supporting Information) within this $p(O_2)$ range (Figure 4a).

The number of free carriers continues to steadily increase at lower oxygen content; at the same time, indium atoms with very low coordination may pair up forming short-distant metal–metal bonds—provided that there are no oxygen atoms available to be shared between these low-coordinate In atoms. The strongly localized defects associated with a trapped electron at the M–M bond, appear below the conduction band edge—once the [O]/[M] ratio is smaller than a certain composition-specific threshold. For undoped indium oxide, the threshold corresponds to theoretical oxygen stoichiometry $In_2O_{3-\delta}$ with $\delta = 0.08$ in the structures simulated with MD quench rate of 200 K ps^{-1} and to experimental $p(O_2) = 7$ mTorr in PLD-grown samples of 270–380 nm thickness deposited at $T_d = -25$ °C. It is important to stress that the deposition technique and conditions as well as the cation composition are expected to have a significant effect on the defect formation in AOSs. In addition, post-deposition annealing is an effective tool to improve the carrier mobility in AOSs since the extra energy due to heating allows the amorphous network to reorganize (e.g., via oxygen diffusion) in order to better accommodate the irregular charge density distribution and, hence, to suppress the strongly localized defects.

The formation of tail states near the top of the valence band associated with under-coordinate oxygen atoms[87] is also governed by the [O]/[M] ratio. For the three amorphous structures of indium oxide; that is, the perfectly stoichiometric In_2O_3 as well as $In_2O_{2.96}$ and $In_2O_{2.92}$ (Figure 3a), the localization of the tail states decreases with increased oxygen stoichiometry—an opposite trend to the localization of the conduction band defects. Indeed, at larger [O]/[M] ratios, the increased number of fully coordinate metal atoms screens an under-coordinate oxygen defect more effectively, leading to a stronger localization of the corresponding tail states above the valence band edge.

Thus, the formation of both the valence and conduction band defects is intrinsically interconnected (Figure 4b); tuning the [O]/[M] ratio that governs the defect concentration as well as the degree of localization of the defects will ensure an optimal electrical and optical performance in AOSs.

5. Role of Cation Composition in Structure and Properties of AOSs

5.1. Local Structure and Amorphization Efficiency

In multicomponent AOSs, two or more binary oxides are mixed during the deposition to facilitate the formation of an amorphous state at room temperature. As expected, structural disorder increases with the substitution level in ternary and quaternary AOSs; however, there is no clear understanding regarding the role played by the individual metal species in the formation of amorphous state and the AOSs properties. Most research has focused on quaternary oxides such as a-In-Ga-Zn-O or a-Zn-In-Sn-O given their technological appeal;[48,49,51–57,62–66,68,69,73,74,76] only a few studies addressed the properties of ternary AOSs systematically.[67,85,86] Moreover, a comparison of the results available in the literature is likely to be inconclusive because the crystallization temperature

© 2017 The Authors. Published by WILEY-VCH Verlag GmbH & Co. KGaA, Weinheim

depends strongly not only on the metal composition but also on growth conditions (such as oxygen partial pressure, post-deposition temperatures and times) as well as film thickness.

To understand the underlying microscopic mechanisms that govern the amorphization process in post-transition metal oxides, the local and medium-range structural features of amorphous In–X–O with 20% fractional substitution of X = Ga, Zn, or Sn (labeled a-IGO, a-IZO, or a-ITO hereafter) are systematically compared to those in amorphous indium oxide (a-IO). All structures were obtained from ab initio MD simulations with the same quench rate of 200 K ps^{-1} and the same oxygen stoichiometry; namely, $(In_2O_{2.96})_{22}(Ga_2O_3)_5$, $(In_2O_{2.96})_{22}(ZnO)_{10}$, and $(In_2O_{2.96})_{22}(SnO_2)_{10}$, which was set in all structures prior to quenching. It is found that the addition of Ga_2O_3, ZnO, or SnO_2 into the indium oxide host i) increases the local distortions of the InO polyhedra as signified by a larger variance for the first-shell In-O distances, 1.07×10^{-2} Å^2, 1.05×10^{-2} Å^2, or 1.24×10^{-2} Å^2 in a-IGO, a-IZO, or a-ITO, respectively—as compared to $\sigma^2 = 8.42 \times 10^{-3}$ Å^2 in amorphous indium oxide; and ii) suppresses the number of high-coordinate In atoms (the effective coordination number 5.5 or above) from 44% in amorphous indium oxide to 23% in a-IGO and a-ITO and to 9% in a-IZO (note that a single amorphous structure from an MD simulation at 300 K or from a DFT-optimized solution at 0 K tend to overestimate the In–O coordination in a–In–X–O with X = Ga or Zn as compared to amorphous indium oxide[92,93] in contrast to the time average presented here). The smallest amount of the fully coordinate In atoms in a-IZO is in accord with the highest crystallization temperature measured experimentally in In-Zn-O with 10% of zinc; namely, 630 °C. For comparison, the crystallization temperature; that is, the temperature at which the bixbyite In_2O_3 fraction exceeds 80%, is measured to be 120 °C in undoped amorphous indium oxide, 450 °C for 20% of Ga substitution, and only 160 °C for 10% of Tin, all grown by PLD under the same oxygen pressure of 8 mTorr.

The experimental trend in the crystallization temperature (T_{cryst}(ITO) << T_{cryst}(IGO) < T_{cryst}(IZO)) cannot be explained by the aforementioned changes in the local first-shell In–O structure alone. One needs to look at the local structure of the XO polyhedra, although the T_{cryst} trend does not appear to directly correlate with the strength of the metal–oxygen bond of the added metal (Sn–O < Zn–O << Ga–O). The results of our MD simulations for amorphous In–X–O provide the following insights: i) In marked contrast to the under-coordinated In atoms, the majority of the X cations attain their natural coordination; that is, the coordination in the corresponding crystalline binary or ternary oxides; namely, 4 for Zn, 6 for Sn, and 4, 5 or 6 for Ga (**Figure 5**). ii) At room temperature, the oxygen coordination is "frozen" for most of the X cations: the coordination variance averaged over the MD time period of 6 ps is 0.07 for Ga atoms, 0.06 for Sn, and 0.11 for Zn at 300 K. These values are notably smaller than the average variance for the In coordination; namely, 0.14 in a-IGO or a-IZO and 0.15 in a-ITO, also calculated at 300 K. iii) Most importantly, the X cations behave differently once the temperature is increased (Figure 5b), in contrast to Tin atoms, where the calculated coordination variance remains small even at 500 K; namely ≤0.11, the average variance in the Zn–O coordination is almost two times larger, 0.19 at 500 K. For Ga atoms, the average coordination variance is 0.16 at 500 K, making the trend in the calculated coordination variance (Sn–O in ITO < Ga–O in IGO < Zn–O in IZO) to be in accord with the observed crystallization temperature in In–X–O for X = Sn, Ga, and Zn. The large deviations in the coordination of particular Ga or Zn atoms at high temperature arise from the ability of these cations to adopt to several oxygen environments. Specifically, while Zn atoms are 4-coordinate in wurtzite ZnO and Ga atoms are 4 and 6-coordinate in monoclinic β-Ga_2O_3, both are 5-coordinate in crystalline $InGaZnO_4$.[40] Thus, the large deviations in the Ga–O and Zn–O coordination associated with the multi-coordinate nature of these cations, along with the ability of the host atoms to easily adjust to a changing oxygen environment, help maintain the disorder in these In-based AOSs at high temperatures.

Another important factor governing the amorphization process is the medium-range structural preferences of the added metal atoms; that is, sharing of the XO polyhedra and the resulting spatial distribution of differently coordinated InO and XO polyhedra. In accord with the observed low effectiveness of tin to amorphize indium oxide structure, the number and the distribution of edge- and corner-shared MO polyhedra obtained from MD simulations deviates insignificantly from those in undoped amorphous indium oxide (Figure 5c). This finding stems from the similarities in the electronic configuration, ionic size, and oxygen coordination preferences of Sn and In cations. Moreover, the majority (over 60%) of the introduced edge-shared connections with short M–M distances, 3.0–3.2 Å (Figure 5c) involve Sn atoms. This result signifies that tin has a tendency to promote clustering, especially at high concentration of Sn (that also limits the carrier mobility of a-ITO,[93] as discussed in Section 5.3 below). In marked contrast to Sn, the addition of both Ga and Zn not only suppresses the edge-sharing peak in the M–M distribution, but also leads to a much broader range of the corner-shared M–M pairs. As a result, the edge- and corner-sharing peaks overlap completely (Figure 5c), suggesting that the medium-range disorder in a-IZO and a-IGO increases as compared to that in a-IO and a-ITO. Experimentally, the second and third shells cannot be fitted in this case; the corresponding structures are often called EXAFS-free amorphous.[67]

Last but not least, an internal strain introduced by the presence of additional cations may also affect amorphization. A systematic experimental and theoretical study of the amorphous indium oxide doped with group III metals, Sc, Y, and La, showed that the amorphization efficiency increases with the size of the ionic radius of the substituted cation.[67] The local structure comparison of the amorphous In–X–O with 20% substitution of X = Sc, Y, or La have revealed that scandium is too small to suppress the amount of InO_6 polyhedra and to prevent their clustering, whereas lanthanum is large enough to make the In–La–O samples fully X-ray amorphous—even with only 5% La doping in films processed at 300 °C.[67]

While a theoretical calculation of the crystallization temperature in a-In–X–O is beyond the scope of this work, the above results of the MD liquid-quench simulations clearly illustrate that complex interplay between the local and medium-range structural preferences of both the host and the substitution metals must be taken into account in the search for efficient amorphizers.

© 2017 The Authors. Published by WILEY-VCH Verlag GmbH & Co. KGaA, Weinheim

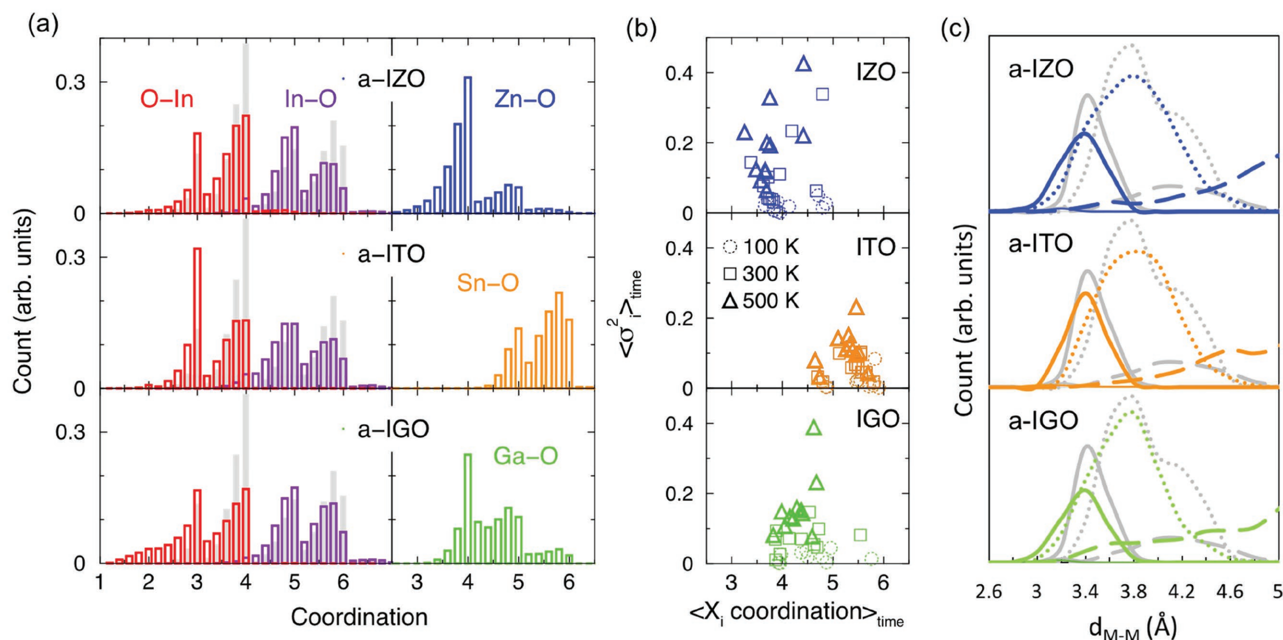

Figure 5. Structural properties of amorphous In–X–O with 20% fractional substitution of X = Ga, Zn, or Sn. The structures were obtained from ab initio MD simulations with quench rate of 200 K ps^{-1}; the oxygen stoichiometry is 2.96. a) Distribution of differently coordinated In, O, or X atoms in a-In–X–O. Coordination distribution in amorphous indium oxide is given for comparison as grey bars. b) The coordination of X atoms averaged over time as obtained from MD simulations at 100 K (circle), 300 K (square), or 500 K (triangle). c) Distribution of the edge-shared (solid line), corner-shared (dotted line), and non-shared (dashed line) M–M neighbors as a function of the metal–metal distance in amorphous IZO (blue), ITO (orange), IGO (green), and IO (grey).

5.2. Carrier Generation in Multi-Cation AOSs

One of the major differences between the multi-cation crystalline and amorphous oxide semiconductors concerns carrier generation. In striking contrast to crystalline TCOs where external aliovalent doping is the most viable way to generate free carriers and to control the carrier concentration over a wide range (from 10^{17} to 10^{21} cm^{-3}), additional cations in AOSs do not act as carrier donors or acceptors. This is evident from the following: i) for amorphous In–X–O with as much as 30% substitution of X = Ga, Zn, or Sn, grown by PLD using a deposition temperature of T_d = –25 °C and an oxygen partial pressure of 8 mTorr, the measured carrier concentration, $n = 0.8 \times 10^{20}$ cm^{-3}, 1.2×10^{20} cm^{-3}, or 1.6×10^{20} cm^{-3}, respectively, is similar or, in the case of a-ITO, identical to that in undoped amorphous indium oxide grown under the same deposition conditions, $n = 1.6 \times 10^{20}$ cm^{-3};[93] and ii) our calculated electronic band structure of stoichiometric amorphous ternary In–X–O or quaternary In–Ga–Zn–O, Zn–In–Sn–O, etc, oxides corresponds to an insulator—independent of the level of fractional substitution and the valence of added cation(s) with respect to the valence of the host cation.

The fact that aliovalent cation(s) in In-based AOSs do not serve as free electron dopants stems from an ability of the cations to attain their preferred local oxygen environment—an advantage provided by the amorphous structure with many degrees of freedom. A structural analysis of amorphous In–X–O with 20% of X = Ga, Sn, or Zn obtained using ab initio MD simulations, shows that the XO polyhedra are highly distorted—as signified by the average variance of the first-shell X–O distances, namely, 1.89×10^{-2} Å^2, 0.91×10^{-2} Å^2, or 1.34×10^{-2} Å^2 in a-IGO, a-ITO or a-IZO, respectively, being comparable to those for the In–O distances in these ternary structures, $\sigma^2 = 1.1 - 1.2 \times 10^{-2}$ Å^2. Despite the strong local distortions, the X cations tend to have high coordination with oxygen atoms: as mentioned in the previous section, most of the X atoms attain their natural coordination; that is, the one found in the corresponding crystalline binary (4 for Zn; 6 for Sn; and 4 or 6 for Ga, as in monoclinic β-Ga_2O_3) or multi-cation oxides (for example, both Ga and Zn have 5-fold coordination with oxygen in crystalline $InGaZnO_4$). In a-In–X–O with 20% of X = Ga, Sn, or Zn, the majority of Zn and Sn atoms are four and six coordinated, respectively (Figure 5). In a-IGO, about two thirds of the Ga atoms are four coordinate, while the coordination of the rest of the Ga atoms is equally distributed between above 4.0 and below 5.0 (Figure 5). Similarly, it has been found that adding 20% of GeO_2, Sc_2O_3, Y_2O_3, or La_2O_3 into indium oxide melt, resulted in Ge, Sc, Y, or La reaching their natural coordination upon the MD quenching of the amorphous oxides.[92] The fulfilled coordination with oxygen atoms is in accord with the stronger bonding between the oxygen and the added metal species with respect to that of the host metal; that is, the In–O bonds.

In contrast to the fully coordinate minority cations in the amorphous In–X–O, the average coordination of indium is reduced from 5.3 in a-IO to 5.1 in a-IGO and to 5.0 in a-ITO and a-IZO. The presence of X leads to an increased number of low-coordinate In atoms (with the coordination number 5.0 or below) as compared to that in amorphous indium oxide; moreover, for many of the indium atoms the coordination varies by

© 2017 The Authors. Published by WILEY-VCH Verlag GmbH & Co. KGaA, Weinheim

as much as 2, for example, between 4 and 6, within a 6 ps time period at room temperature. The electronic structure calculations of non-stoichiometric amorphous In–X–O (with oxygen stoichiometry similar to that considered in a-$In_2O_{2.96}$; c.f., Figure 3a–f) confirm that indium remains to serve as the main source of donor defects upon fractional substitution with X. The calculated charge density distribution in the partially occupied conduction band reveals that among all possible metal–metal nearest neighbor pairs, the largest charge value belongs to two In atoms that are under-shared and have low-coordination with oxygen atoms: for all three compositions considered; that is, for In–X–O with X = Ga, Sn, or Zn, the coordination number for both In atoms is 4.6 – 4.8, the In–In distance is 3.2 – 3.4 Å, and the two indium atoms are corner shared; that is, missing the second oxygen atom the two are supposed to share at this separation typical of edge-shared polyhedra. These structural features of the oxygen-depleted region resulting in a notable conduction charge accumulation in amorphous In–X–O, are similar to those found in undoped amorphous indium oxide at the same oxygen stoichiometry (see Section 4 and Figure 3a–f).

Importantly, our theoretical results support the weak dependence of the experimental carrier concentration on the composition in amorphous ternary In-based oxides.[93] The electronic structure calculations for the amorphous non-stoichiometric In–X–O with 20% of X show that the cation composition has little effect on the conduction states below the Fermi level and on the free carrier concentration: i) similar to a-IO (Figure 3), the defect state remains to be shallow as seen from the low value of the inverse participation ratio for the occupied states in the conduction band of amorphous In–X–O (**Figure 6**); and ii) the Burstein–Moss (BM) shift; that is, the Fermi level shift into the conduction band, is 1.40 eV in a-ITO, 1.46 eV in a-IGO, and 1.51 eV in a-IZO, that is only slightly smaller than the shift in a-IO, 1.61 eV, with the same oxygen stoichiometry. Moreover, additional calculations for an amorphous structure with larger Ga fraction, $In_{1.2}Ga_{0.8}O_{2.96}$, where a BM shift of 1.55 eV and a shallow donor state are obtained, further illustrate the weak dependence of the number of free carriers on the cation composition in AOSs with high oxygen stoichiometry (> 2.96). Understanding the role of composition in the formation of deep defects in multi-cation In-based amorphous oxides with lower oxygen content (oxygen stoichiometry < 2.96) is a next step and will be discussed elsewhere.

5.3. Electron Localization and Carrier Mobility

Although the presence of additional cations in In-based AOSs does not govern the free carrier generation, composition-induced differences in the oxygen-sharing and medium-range spatial distribution of the differently coordinate InO and XO polyhedra affect the carrier mobility. First of all, in contrast to the undoped indium oxide where a three-fold change in the Hall mobility is observed above and below the transition to a fully amorphous state, as described in Section 3 above, the mobility in In–X–O is expected to have a weaker dependence on the deposition temperature—owing to the suppressed amount of the InO_6 polyhedra in the ternary oxides (Figure 5a) and, hence, a decreased probability of InO_6 chain formation (see Section 3 and Figure 2b). From experimental observations, for IZO with 15% ZnO grown at an oxygen partial pressure of 8 mTorr, the mobility stays at 60 $cm^2 V^{-1} s^{-1}$ for the deposition temperatures T_d = 25 °C, 100 °C, and 200 °C. Once the crystalline fraction starts to increase (above 200 °C), the mobility gradually drops to 30 $cm^2 V^{-1} s^{-1}$ at T_d = 400 °C. An even weaker dependence of the carrier mobility on the deposition temperature is found in ITO with 15% SnO_2: the mobility varies within 40 – 50 $cm^2 V^{-1} s^{-1}$ for the deposition temperatures –25 °C, 25 °C, 50 °C, 100 °C, and 200 °C; that is, well below and above the transition to fully amorphous state with no X-ray peaks observed at T_d = 50 °C and below. From a technological point of view, a wider range of the deposition temperatures for which the mobility is maintained, makes the multi-cation AOSs more appealing as compared to undoped amorphous indium oxide.

When the substitutional doping level in multicomponent AOSs increases, clustering of fully coordinate X cations leads to a non-uniform charge density distribution for the conduction states and, therefore, to a variable range hopping[94] through the states of different energy. Accurate DFT-based hybrid-functional calculations of amorphous In–X–O with 20% fractional substitution of X = Ga, Zn, or Sn, reveal that the localization above the Fermi level is strongest in In–Ga–O, followed by In–Sn–O, In–Zn–O, and then In–O—in excellent agreement with the observed trend of the Hall carrier mobility measured as a function of fractional substitution (0 – 30%) in amorphous In–X–O (Figure 6c). The calculated charge density distribution for the energy slice of 0.5 eV above the Fermi level (unoccupied states) illustrates (Figure 6b) that an extra free electron is likely to get trapped at the under-coordinate In atom surrounded by three Ga atoms, all of which have their coordination fully satisfied. Similar to the a-IO case where the electron density near the Fermi level avoids the six-coordinate InO_6 (c.f., Figure 2d and e), the empty states of the four-coordinate Ga atoms have a higher energy and, hence, are not available for the conduction electron to propagate.

To further understand the role of different cation species in carrier transport of amorphous In–X–O, the conduction charge density (for the unoccupied states within 0.5 eV above the Fermi level) is calculated along all metal–metal nearest neighbors and the results are compared for In–In, In–X, X–In and X–X pairs in each structure. It is found that, independent of doping, the average charge density values for the In–In neighbors are nearly identical for X = Ga, Sn, and Zn, whereas the contributions from X–In and X–X pairs are cation-specific: on average, the charge density is large near Sn atoms (slightly larger than that for In–In neighbors), almost two times smaller near Zn, and even smaller near Ga (Figure 6d). The non-uniform charge density distribution in the conduction states of multi-cation AOSs is associated with i) different strength of the metal–oxygen bonds; ii) different M–O coordination and the degree of local distortions in the MO polyhedra; as well as iii) spatial distribution of the MO polyhedra, e.g., clustering of GaO_x vs. chain formation of InO_6–SnO_6 vs. random distribution of ZnO_4.[93] All the above local and medium-range structural features ultimately determine the energy profile of the conduction states and are responsible for the complex nature of the carrier mobility in multicomponent AOSs.

© 2017 The Authors. Published by WILEY-VCH Verlag GmbH & Co. KGaA, Weinheim

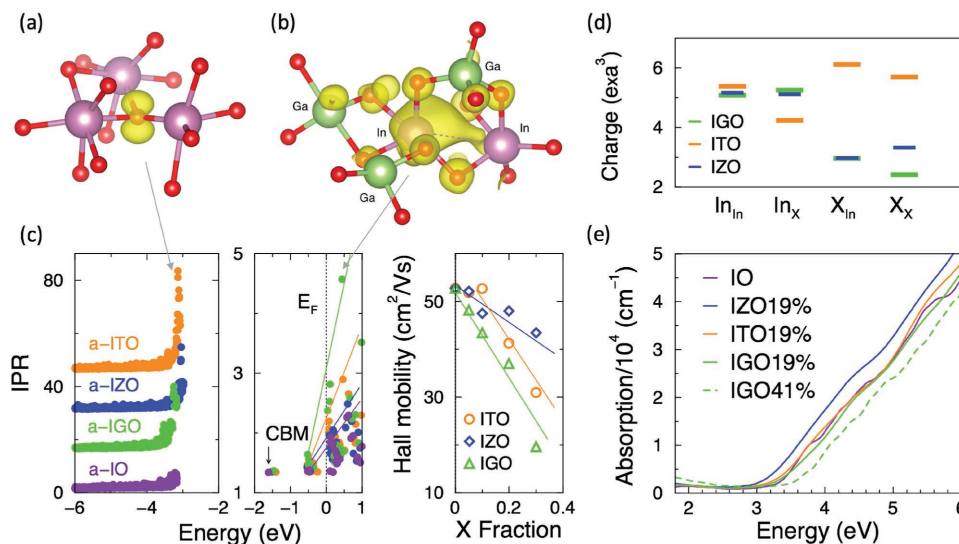

Figure 6. Electronic properties of amorphous In–X–O with 20% of fractional substitution of X = Ga, Zn, or Sn. The structures were obtained from ab initio MD simulations with quench rate of 200 K ps^{-1} and optimized using DFT-GGA approximation; the electronic structure was calculated using hybrid HSE functional. a) The calculated charge density distribution for the tail defect state at the top of the valence band in a-In–Sn–O. b) The charge density distribution calculated in the energy slice of 0.5 eV above the Fermi level in a-In–Ga–O. c) The calculated inverse participation ratio in a-In–X–O structures for the valence (left panel) and conduction bands (middle panel). The Fermi level is at 0 eV. Experimental Hall mobility in amorphous In–X–O as a function of fractional substitution of X (right panel). The samples were obtained using PLD at deposition temperature T_d = –25 °C and with oxygen partial pressure of 8 mTorr. d) Charge density contributions calculated along the In–In, In–X, X–In and X–X bonds in In–X–O: the average charge values near the first metal atom in the given pair are shown. e) Calculated optical absorption as a function of composition in non-stoichiometric amorphous IO ($In_2O_{2.96}$) and In–X–O (IZO19% = $(In_2O_{2.96})_{22}(ZnO)_{10}$, ITO19% = $(In_2O_{2.96})_{22}(SnO_2)_{10}$, IGO19% = $(In_2O_{2.96})_{22}(Ga_2O_3)_5$, and IGO41% = $(In_2O_{2.94})_{16}(Ga_2O_3)_{11}$).

5.4. Tail States and Optical Band Gap as a Function of Composition

From a technological point of view, the wide range of fractional compositions in ternary and quaternary AOSs is highly appealing for tuning the optical band gap and work function in these multifunctional materials.[95,96] First, the effect of cation composition on the tail states near the top of the valence band of AOSs is generalized.[73] As mentioned in Section 4, a strongly localized state is formed when an under-coordinate oxygen atom is surrounded by fully-coordinate metal atoms resulting in a charge imbalance. In amorphous In–X–O with 20% of X = Ga, Zn, or Sn, the number of under-coordinate oxygen atoms increases as compared to undoped amorphous indium oxide (c.f., Figure 3a)—and so does the electron localization at the defect states near the valence band maximum (Figure 6c). With over 30% of three-coordinate oxygen atoms in a-In–Sn–O, the localization of the tail states is the strongest in this case. As shown in Section 4, the tail states contribute to the optical absorption at 2–3 eV for stoichiometric a-IO (Figure 3c). When the [O]/[M] ratio is reduced, the number of fully coordinate metal atoms decreases and, consequently, both the concentration of such defects as well as the degree of the electron localization caused by the defects are suppressed.

The presence of valence band tail states becomes irrelevant for the optical transmission of under-stoichiometric AOSs—owing to the pronounced Burstein–Moss shift upon the degenerate doping. From the accurate DFT-based hybrid-functional calculations of the real and imaginary dielectric function for amorphous In–X–O with 20% fractional substitution of X = Ga, Zn, or Sn, it is found that all three compositions demonstrate low optical absorption within the visible range; that is, for 1.8–3.0 eV (Figure 6e). Compared to amorphous indium oxide obtained with the same MD quench rate and the same oxygen stoichiometry as the In–X–O structures, addition of 20% of zinc reduces the optical band gap by 0.2 eV, whereas the same fraction of tin or gallium has no effect on the optical absorption edge and the gap remains equal to 3.2 eV (Figure 6e). As expected, larger substitutional fraction of Ga opens up the transparency window: the optical band gap for amorphous $In_{1.19}Ga_{0.81}O_{2.94}$ is 3.5 eV. Thus, cation composition is an indispensable tool to manipulate the crystallization, carrier transport, as well as optical band gap of multicomponent AOSs.

6. Structure and Properties of AOSs under Strain

Another important technological advantage of AOSs is their mechanical flexibility: the amorphous oxides are bendable and maintain their excellent optical and electrical properties under the strain.[97] The superior mechanical properties of AOSs over their crystalline counterparts that are brittle make the amorphous oxide semiconductors an attractive candidate for flexible transparent electronics.

To understand how the structural, electronic, and optical properties of AOSs change under strain, amorphous In_2O_3 and $Zn_{0.30}In_{1.40}Sn_{0.30}O_{3.04}$ (a-ZITO) structures were simulated using MD liquid-quench approach with 200 K ps^{-1} rate. Once

© 2017 The Authors. Published by WILEY-VCH Verlag GmbH & Co. KGaA, Weinheim

the amorphous structures were equilibrated at 300 K and optimized within DFT, the volume of the cells was changed to induce lattice strain and the atomic positions of all atoms in the cell were fully relaxed within DFT for each configuration. The structural analysis of the strained a-IO and a-ZITO reveals that the average M–O distances increase slower than expected from the volume expansion (**Figure 7**), suggesting that a structural reorganization has likely occurred.

The coordination of all metal species decreases with strain, albeit differently for each of the metal types (Figure 7d). Among In, Zn and Sn, indium atoms steadily loose oxygen atoms at a highest rate—in accord with its low coordination in amorphous In–Sn–O and In–Zn–O (see Section 4). The average coordination of tin is notably higher than that of indium but only up to the lattice increase of 1.9%; at that point, the Sn–O coordination drops from 5.3 to nearly 5.0 and the amorphous structure breaks—as signified by a discontinuity in the total energy (for comparison, the structure of undoped amorphous indium oxide withstands up to 3% lattice increase; Figure 7a). On the contrary, zinc, having the strongest metal–oxygen bonds in a-ZITO, maintains its coordination of four and even "picks up" the oxygen atoms lost by Sn at the break point.

The first-shell characteristics of the metal constituents—the metal-oxygen bond strength and the preference for specific MO coordination—determine the sharing between the MO polyhedra and, consequently, the response of the medium-range structure to the lattice expansion. As discussed in Section 2 above, the crystalline-to-amorphous transition in amorphous indium oxide suppresses the number of edge-shared InO polyhedra from 50% to 20% giving rise to predominantly corner-shared polyhedra network in the amorphous state. Upon volume expansion, the corner-sharing fraction increases to 90% (Figure 7e). Because corner-shared MO polyhedra with only a single connecting oxygen atom have more degrees of freedom as compared to an edge-shared connection, the corner-shared polyhedral network is capable to respond to the induced volume expansion more efficiently, helping make the amorphous oxide materials fracture-resistant. The ability of the corner-shared M–M connections to absorb the internal lattice stress is likely to be the main reason for the slow increase of the MO distances upon the lattice strain (Figure 7b).

Schematically, the local and medium-range structural changes upon the lattice strain in AOSs can be represented as follows (Figure 7f): i) Initially, two six-coordinated MO polyhedra are connected via two oxygen atoms; that is, are edge-shared. ii) The volume expansion causes one of the polyhedra loose an oxygen atom to become five-coordinate, making the oxygen environment around this under-coordinate metal atom uneven (the cation "sticks out" on one side of the polyhedra). iii) Further volume expansion transforms the M–M connection from edge-shared to corner-shared; this transformation reduces the coordination of the other metal atom from six to five which allows both metal cation to achieve a uniform, charge-balanced oxygen coordination. Thus, strain-induced changes in sharing

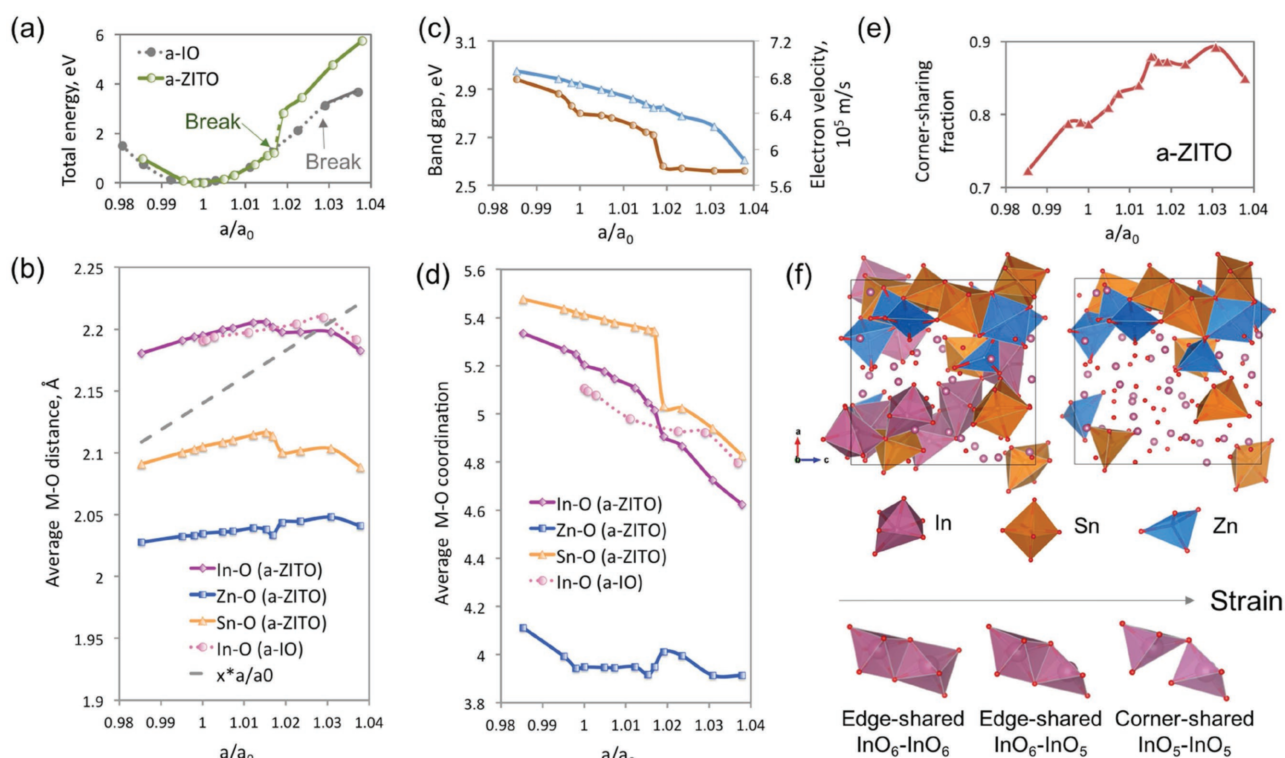

Figure 7. Structural and electronic properties of amorphous In–O (a-IO) and Zn–In–Sn–O (a-ZITO) under strain. The latter amorphous structure with the cation ratio of [In]:[Zn]:[Sn] = 5:1:1 was obtained from ab initio MD simulations with quench rate of 200 K ps^{-1}. Upon the volume change, each structure was optimized using DFT-GGA approximation. a) The calculated total energy as a function of the lattice parameter in a-IO and a-ZITO. b) The average M–O distances; c) the calculated band gap and electron velocity; d) the average M–O coordination; and e) the calculated fraction of corner-shared In–In pairs as a function of the lattice parameter in a-ZITO. f) Structural changes in a-ZITO upon volume expansion.

© 2017 The Authors. Published by WILEY-VCH Verlag GmbH & Co. KGaA, Weinheim

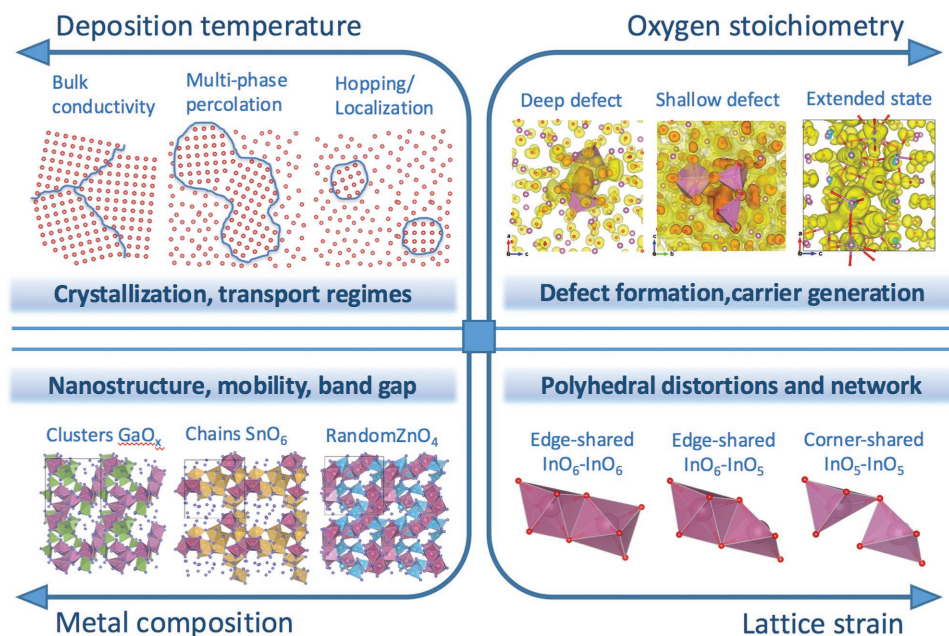

Figure 8. Four-dimensional parameter space for prototype In-based AOSs.

of the MO polyhedra play a crucial role in the mechanical properties of AOSs.

As expected from the longer M–O distances upon the volume expansion, the calculated band gap in strained a-ZITO steadily decreases up to the breaking point (Figure 7c). Above the 1.9% lattice increase, the band gap value remains to be 2.6 eV—consistent with the fact that the average In–O and Sn–O distances slightly shorten at the break point and do not increase further above the break point. The latter finding may be explained by a formation of a void in the amorphous structure upon break, whereas the first-shell M–O distances are maintained, on average. Based on a simple description of the electronic states of a semiconductor using $\boldsymbol{k} \cdot \boldsymbol{p}$ theory,[98] a smaller band gap value should lead to a smaller electron effective mass and a larger electron velocity due to an increased dispersion of the conduction band. In a-ZITO, however, the electron velocity calculated for the amorphous supercell at 0.5 eV above the conduction band minimum, is found to decrease with volume expansion (Figure 7c). The reduction of the electron velocity can be explained based on a comparison of the calculated inverse participation ratio values in the strained a-ZITO: upon the volume expansion, both the IPR value of some states in the conduction band as well as the number of such localized states increase. The formation of such electron-trapping defects is associated with the energy disparity between the differently-coordinated MO polyhedra (for example, fully-coordinate ZnO_4 vs. under-coordinate InO and SnO) that increases with volume expansion. Despite the strain-induced electron localization, both the calculated band gap (2.6–2.9 eV) and the supercell electron velocity ($6–7 \times 10^5$ m s^{-1}) in the amorphous Zn–In–Sn–O remain to be comparable to the values of typical TCOs,[90] suggesting that AOSs retain their excellent optical and electrical properties under strain.

7. Conclusions

The results of systematic ab initio MD simulations, highly precise DFT-based electronic structure calculations, and detailed experimental observations for several In-based oxides are combined into a comprehensive framework to describe the complex microscopic behavior in the prototype AOSs. Four major components that comprise the parameter space of the AOSs (**Figure 8**), namely i) deposition temperature; ii) oxygen stoichiometry; iii) cation composition, and iv) lattice strain, were studied independently. Contingently, the primary role(s) played by each of the four parameters are categorized as follows:

Deposition temperature (or theoretical quench rate) governs the structural and, consequently, the transport regimes during the amorphous to crystalline transition in the oxides. As the structure transforms from nanostructured amorphous to coexistence of crystalline and amorphous phases, and further to crystalline grains, the primary carrier transport mechanism changes from localization, to hopping, to multi-phase percolation and scattering, and further to bulk conductivity, respectively. The developed theoretical model of prototype In-based AOSs provides a fundamental basis for a versatile description of the structural archetypes in these non-periodic oxide systems—from distorted polyhedral network to nano- and microstructure.

Cation composition allows one to control the crystallization temperature and, hence, to fine-tune the degree of amorphization as well as the degree of electron localization governed by composition-dependent characteristics of variable range hopping. Both the substitutional doping level and the type of added metal species have a strong effect on the robustness of the MO chains and the AOSs nanostructure, and therefore, determine the limits of the carrier mobility in the amorphous regime and the range of deposition temperatures for high mobility.

© 2017 The Authors. Published by WILEY-VCH Verlag GmbH & Co. KGaA, Weinheim

Another great technological advantage of the multi-cation AOSs is tunable optical band gap and work function.

Oxygen stoichiometry proves to be the sole mechanism to generate free electrons in AOSs. Given the many degrees of freedom in the amorphous structure, the long-range structural characteristics and the electronic properties of the donor defects in AOSs differ fundamentally from those in their crystalline oxide counterparts. The oxygen/metal ratio controls the formation of structural defects near both band edges of the semiconductor: the concentration as well as the degree of localization of the conduction defects are interrelated to those of the valence tail states. Importantly, the results show that defects in AOSs require full MD simulation and cannot be modeled with simple post-quench oxygen vacancies.

Lattice strain associated with external or internal stress (e.g., due to flexible organic substrate, thin film geometry, or mismatched cation size) affects the local distortions in the MO polyhedra as well as in the polyhedral network and may further enhance the effects of deposition temperature, oxygen stoichiometry, or cation composition on the defect formation[99] as well as on the transport and optical properties of AOSs.

The thorough microscopic understanding gained within the framework of this four-dimensional parameter space of the In-based AOSs, serves as a solid foundation for i) finding an optimal set of parameters to tailor the electrical, optical, thermal, and mechanical properties of AOSs for specific applications, enhancing the utility of these materials for practical devices; and ii) exploring possible ways to extend the phase space of known AOSs by including novel anion and cation compositions toward next-generation amorphous semiconductors.

8. Experimental Section

Theoretical calculations: The amorphous oxide structures were generated using first-principles molecular-dynamics (MD) liquid-quench simulations as implemented in the Vienna Ab Initio Simulation Package (VASP).[100–103] The calculations are based on the density functional theory (DFT) with periodic boundary conditions and employ PBE functional[104] within the projector augmented-wave method.[105,106] A bixbyite cell of In_2O_3 with crystalline density of 7.12 g cm^{-3} and with 80 (or 134) atoms per cell was used as initial structure which was melted at 3000 K to eliminate any crystalline memory. To model non-stoichiometric indium oxide, oxygen atoms were randomly removed from the melt and the new structures were kept at 3000 K for additional 5–10 ps to randomize the configuration. Similarly, for doped indium oxide, random In atoms were substituted with a specific fraction of Ga, Sn, or Zn, and the cell density as well as the oxygen/metal ratio were adjusted prior to additional melting. Specifically, the density of In–X–O with 20 at% X was 6.90 g cm^{-3}, 6.99 g cm^{-3}, and 6.75 g cm^{-3} for X = Ga, Sn, and Zn, respectively. For each of the In-based oxide melt, liquid quench simulations were performed as follows. The structure was cooled to 1700 K at the MD rate of 100 K ps^{-1} and then rapidly quenched to 100 K with a desired rate (5–900 K ps^{-1}). An energy cut-off of 260 eV and single Γ-point were used during melting and quenching processes. Finally, each structure was equilibrated at 300 K for 6–10 ps with a cut-off energy of 400 eV. All MD simulations were carried out in the NVT ensemble with the Nose–Hoover thermostat using an integration time step of 2 fs. For an accurate structural analysis of the theoretically modeled AOSs, the average pair correlation function and the average effective coordination number were calculated.[107,108] Note that in this work the coordination distribution is obtained as a time average; that is, as an average of the coordination distribution over at least 5000 MD steps at 300 K. The time averaging represents a more reliable approach as compared to the structural analysis of a single amorphous structure by capturing the structural variations at given temperature.

Next, the atomic configurations obtained from the ab initio MD simulations were optimized using the PBE functional.[104] For the optimization, a cut-off energy of 500 eV and the $4 \times 4 \times 4$ Γ-centered *k*-point mesh were used; the atomic positions were relaxed until the Hellmann–Feynman force on each atom was below 0.01 eV Å^{-1}. The electronic and optical properties of amorphous In-based oxides were calculated using the hybrid Heyd-Scuseria-Ernzerhof (HSE06) approach[109,110] with a mixing parameter of 0.25 and a screening parameter μ of 0.2 Å^{-1}. To characterize the localization of the electronic states within the band gap and near the band edges, the inverse participation ratio (IPR) was calculated. Optical absorption was derived from the frequency-dependent dielectric function, $\varepsilon(\omega) = \varepsilon_1(\omega) + i\varepsilon_2(\omega)$, calculated within independent particle approximation as implemented in VASP. The imaginary part, $\varepsilon_2(\omega)$, is related to the optical absorption at a given frequency ω, and is determined based on the electronic transitions of the hybrid functional solution. The real part of the complex dielectric function is obtained using Kramers-Kronig relations.

The structural properties and charge density distribution in amorphous oxides were analyzed and plotted using VESTA.[111]

Experimental procedure: Amorphous oxide thin films were grown by pulsed-laser deposition (PLD) from a dense hot-pressed indium oxide, zinc oxide, tin oxide, and gallium oxide targets (25 mm diameter). PLD was accomplished with a 248 nm KrF excimer laser with 25 ns pulse duration and operated at 2 Hz. The 200 mJ per pulse beam was focused onto a 1 mm × 3 mm spot size. Less than 1 monolayer is deposited during each In_2O_3/XO PLD cycle to ensure mixing at the atomic-layer level. The target was rotated at 5 rpm about its axis to prevent localized heating. The target–substrate separation was fixed at 10 cm. For multicomponent films the appropriate basis-oxide targets were employed. A computer controlled shuttle was used to alternate ablation between targets. Less than one monolayer of material was deposited in a typical cycle between the targets to help ensure uniformity of film composition; the ratio of the pulses for each metal oxide in each cycle was adjusted to obtain the desired film composition. The compositions reported are nominal compositions: the ratio of the number of dopant pulses to total pulses. The films were grown on silicon substrates in an O_2 ambient varied from 1 mTorr to 16 mTorr. The substrates were attached to the substrate holder with silver paint and grown at a deposition temperature specified in the text or figure caption. Films grown above 25 °C were attached to a resistively heated substrate holder; films grown below 25 °C were attached to a liquid nitrogen cooled substrate holder. Sheet resistance (R_s: Ω □$^{-1}$), carrier type, area carrier-concentration (n_a: 1 cm^{-2}), and carrier mobility (μ_{hall}: cm^2 V^{-1} s^{-1}) were measured with a Ecopia 3000 Hall measurement system on samples in the van der Pauw geometry. Carrier density (n_v: 1 cm^{-3}) and resistivity (ρ: Ω cm) were calculated by dividing the area carrier concentration and sheet resistance, respectively, by the film thickness. Film thickness (d: nm) was measured using a spectral reflectometer (Filmetrics F20).

Supporting Information

Supporting information is available from the Wiley Online Library or from the author.

Acknowledgements

The authors are grateful to Thomas O. Mason for numerous stimulating discussions. Initial simulations for amorphous Zn–Sn–In–O under strain were performed by Rabi Khanal. The work was performed under the collaborative MRSEC program at Northwestern University and supported by the National Science Foundation (NSF) grant DMR-1121262. Computational resources are provided by the NSF-supported XSEDE program and by Department of Energy NERSC facilities.

© 2017 The Authors. Published by WILEY-VCH Verlag GmbH & Co. KGaA, Weinheim

Conflict of Interest

The authors declare no conflict of interest.

Keywords

ab-initio molecular dynamics simulations, amorphous oxide semiconductors, electronic properties, local and medium-range structure, transparent conducting oxides

Received: February 28, 2017
Revised: May 16, 2017
Published online:

[1] K. Bädeker, *Ann. Phys.* **1907**, *22*, 749.
[2] T. G. Bauer, *Ann. Phys.* **1937**, *30*, 433.
[3] C. Bright, *50 Years of Vacuum Coating Technology and the Growth of the Society of Vacuum Coaters*, Society Of Vacuum Coaters, Albuquerque, NM, **2007**.
[4] K. L. Chopra, S. Major, D. K. Pandya, *Thin Solid Films* **1983**, *102*, 1.
[5] A. L. Dawar, J. C. Joshi, *J. Mater. Sci.* **1984**, *19*, 1.
[6] J. R. Bellingham, W. a. Phillips, C. J. Adkins, *J. Mater. Sci. Lett.* **1992**, *11*, 263.
[7] H. L. Hartnagel, A. L. Dawar, A. K. Jain, C. Jagadish, *Semiconducting Transparent Thin Films*, Institute Of Physics Publishing, London, **1995**.
[8] D. S. Ginley, C. Bright, *MRS Bull.* **2000**, *25*, 15.
[9] K. Nomura, *Science* **2003**, *300*, 1269.
[10] P. P. Edwards, A. Porch, M. O. Jones, D. V. Morgan, R. M. Perks, *Dalton Trans.* **2004**, 2995.
[11] G. J. Exarhos, X.-D. Zhou, *Thin Solid Films* **2007**, *515*, 7025.
[12] E. Fortunato, D. Ginley, H. Hosono, D. C. Paine, *MRS Bull.* **2007**, *32*, 242.
[13] J. F. Wager, D. A. Keszler, R. E. Presley, *Transparent Electronics*, Springer US, Boston, MA, **2008**.
[14] *Transparent Electronics: From Synthesis to Applications*, (Eds: A. Facchetti, T. J. Marks), John Wiley And Sons, Hoboken, NJ, **2010**.
[15] *Handbook of Transparent Conductors*, Eds: D. S. Ginley, H. Hosono, D. C. Paine), Springer US, Boston, MA, **2011**.
[16] P. Barquinha, R. Martins, L. Pereira, E. Fortunato, *Transparent Oxide Electronics: From Materials to Devices*, John Wiley And Sons, Hoboken, NJ, **2012**.
[17] K. Ellmer, *Nat. Photonics* **2012**, *6*, 808.
[18] E. Fortunato, P. Barquinha, R. Martins, *Adv. Mater.* **2012**, *24*, 2945.
[19] X. Yu, T. J. Marks, A. Facchetti, *Nat. Mater.* **2016**, *15*, 383.
[20] H. Ohta, H. Hosono, *Mater. Today* **2004**, *7*, 42.
[21] T. Minami, *MRS Bull.* **2000**, *25*, 38.
[22] S. Calnan, A. N. Tiwari, *Thin Solid Films* **2010**, *518*, 1839.
[23] R. D. Shannon, J. L. Gillson, R. J. Bouchard, *J. Phys. Chem. Solids* **1977**, *38*, 877.
[24] A. J. Freeman, K. R. Poeppelmeier, T. O. Mason, R. P. H. Chang, T. J. Marks, *MRS Bull.* **2000**, *25*, 45.
[25] T. Moriga, D. R. Kammler, T. O. Mason, G. B. Palmer, K. R. Poeppelmeier, *J. Am. Ceram. Soc.* **1999**, *82*, 2705.
[26] H. Kawazoe, K. Ueda, *J. Am. Ceram. Soc.* **1999**, *82*, 3330.
[27] M. P. Taylor, D. W. Readey, C. W. Teplin, M. F. A. M. van Hest, J. L. Alleman, M. S. Dabney, L. M. Gedvilas, B. M. Keyes, B. To, J. D. Perkins, D. S. Ginley, *Meas. Sci. Technol.* **2005**, *16*, 90.
[28] P. F. Ndione, Y. Shi, V. Stevanovic, S. Lany, A. Zakutayev, P. A. Parilla, J. D. Perkins, J. J. Berry, D. S. Ginley, M. F. Toney, *Adv. Funct. Mater.* **2014**, *24*, 610.
[29] J. G. Labram, Y.-H. Lin, T. D. Anthopoulos, *Small* **2015**, *11*, 5472.
[30] H. Kawazoe, M. Yasukawa, H. Hyodo, M. Kurita, H. Yanagi, H. Hosono, *Nature* **1997**, *389*, 939.
[31] R. Nagarajan, A. D. Draeseke, A. W. Sleight, J. Tate, *J. Appl. Phys.* **2001**, *89*, 8022.
[32] Y. Ogo, H. Hiramatsu, K. Nomura, H. Yanagi, T. Kamiya, M. Hirano, H. Hosono, *Appl. Phys. Lett.* **2008**, *93*, 32113.
[33] O. Mryasov, A. Freeman, *Phys. Rev. B* **2001**, *64*, 233111.
[34] Ç. Kılıç, A. Zunger, *Phys. Rev. Lett.* **2002**, *88*, 95501.
[35] C. G. Van de Walle, *Phys. Status Solidi B* **2002**, *229*, 221.
[36] S. Lany, A. Zunger, *Phys. Rev. Lett.* **2007**, *98*, 45501.
[37] A. Murat, A. U. Adler, T. O. Mason, J. E. Medvedeva, *J. Am. Chem. Soc.* **2013**, *135*, 5685.
[38] H. Mizoguchi, P. M. Woodward, *Chem. Mater.* **2004**, *16*, 5233.
[39] J. E. Medvedeva, *Europhys. Lett.* **2007**, *78*, 57004.
[40] J. E. Medvedeva, C. L. Hettiarachchi, *Phys. Rev. B – Condens. Matter Mater. Phys.* **2010**, *81*, 125116.
[41] A. Walsh, J. L. F. Da Silva, S.-H. Wei, *J. Phys. Condens. Matter* **2011**, *23*, 334210.
[42] A. Murat, J. E. Medvedeva, *Phys. Rev. B – Condens. Matter Mater. Phys.* **2012**, *86*, 085123.
[43] J. E. Medvedeva, A. J. Freeman, *Europhys. Lett.* **2005**, *69*, 583.
[44] J. E. Medvedeva, *Appl. Phys. A Mater. Sci. Process.* **2007**, *89*, 43.
[45] J. E. Medvedeva, *Phys. Rev. Lett.* **2006**, *97*, 086401.
[46] A. Walsh, J. L. F. Da Silva, S. H. Wei, C. Körber, A. Klein, L. F. J. Piper, A. Demasi, K. E. Smith, G. Panaccione, P. Torelli, D. J. Payne, A. Bourlange, R. G. Egdell, *Phys. Rev. Lett.* **2008**, *100*, 167402.
[47] G. Hautier, A. Miglio, G. Ceder, G.-M. Rignanese, X. Gonze, *Nat. Commun.* **2013**, *4*, 2292.
[48] K. Nomura, H. Ohta, A. Takagi, T. Kamiya, M. Hirano, H. Hosono, *Nature* **2004**, *432*, 488.
[49] H. Hosono, *J. Non. Cryst. Solids* **2006**, *352*, 851.
[50] B. Yaglioglu, H.. Yeom, R. Beresford, D. C. Paine, *Appl. Phys. Lett.* **2006**, *89*, 62103.
[51] J. C. Park, S. Kim, S. Kim, C. Kim, I. Song, Y. Park, U. I. Jung, D. H. Kim, J. S. Lee, *Adv. Mater.* **2010**, *22*, 5512.
[52] T. Kamiya, H. Hosono, *NPG Asia Mater.* **2010**, *2*, 15.
[53] T. Kamiya, K. Nomura, H. Hosono, *Sci. Technol. Adv. Mater.* **2010**, *11*, 44305.
[54] J. S. Park, W.-J. Maeng, H.-S. Kim, J.-S. Park, *Thin Solid Films* **2012**, *520*, 1679.
[55] A. Nathan, S. Lee, S. Jeon, J. Robertson, *J. Disp. Technol.* **2014**, *10*, 917.
[56] J. Y. Kwon, D. J. Lee, K. B. Kim, *Electron. Mater. Lett.* **2011**, *7*, 1.
[57] J. F. Wager, B. Yeh, R. L. Hoffman, D. A. Keszler, *Curr. Opin. Solid State Mater. Sci.* **2014**, *18*, 53.
[58] M. P. Taylor, D. W. Readey, M. F. A. M. van Hest, C. W. Teplin, J. L. Alleman, M. S. Dabney, L. M. Gedvilas, B. M. Keyes, B. To, J. D. Perkins, D. S. Ginley, *Adv. Funct. Mater.* **2008**, *18*, 3169.
[59] M. Ito, M. Kon, C. Miyazaki, N. Ikeda, M. Ishizaki, R. Matsubara, Y. Ugajin, N. Sekine, *Phys. Status Solidi A* **2008**, *205*, 1885.
[60] J. R. Bellingham, W. A. Phillips, C. J. Adkins, *J. Phys. Condens. Matter* **1990**, *2*, 6207.
[61] J. Rosen, O. Warschkow, *Phys. Rev. B* **2009**, *80*, 115215.
[62] A. Takagi, K. Nomura, H. Ohta, H. Yanagi, T. Kamiya, M. Hirano, H. Hosono, *Thin Solid Films* **2005**, *486*, 38.
[63] D.-Y. Cho, J. Song, K. D. Na, C. S. Hwang, J. H. Jeong, J. K. Jeong, Y.-G. Mo, *Appl. Phys. Lett.* **2009**, *94*, 112112.
[64] M. Kimura, T. Kamiya, T. Nakanishi, K. Nomura, H. Hosono, *Appl. Phys. Lett.* **2010**, *96*, 262105.
[65] W. C. Germs, W. H. Adriaans, A. K. Tripathi, W. S. C. Roelofs, B. Cobb, R. A. J. Janssen, G. H. Gelinck, M. Kemerink, *Phys. Rev. B – Condens. Matter Mater. Phys.* **2012**, *86*, 155319.

© 2017 The Authors. Published by WILEY-VCH Verlag GmbH & Co. KGaA, Weinheim

[66] S. Lee, K. Ghaffarzadeh, A. Nathan, J. Robertson, S. Jeon, C. Kim, I.-H. Song, U.-I. Chung, *Appl. Phys. Lett.* **2011**, *98*, 203508.
[67] J. Smith, L. Zeng, R. Khanal, K. Stallings, A. Facchetti, J. E. Medvedeva, M. J. Bedzyk, T. J. Marks, *Adv. Electron. Mater.* **2015**, *1*, 1500146.
[68] H. Godo, D. Kawae, S. Yoshitomi, T. Sasaki, S. Ito, H. Ohara, H. Kishida, M. Takahashi, A. Miyanaga, S. Yamazaki, *Jpn. J. Appl. Phys.* **2010**, *49*, 03CB04.
[69] T. Kamiya, K. Nomura, H. Hosono, *Phys. Status Solidi Appl. Mater. Sci.* **2010**, *207*, 1698.
[70] H. K. Noh, K. J. Chang, B. Ryu, W. J. Lee, *Phys. Rev. B – Condens. Matter Mater. Phys.* **2011**, *84*, 115205.
[71] M. Kim, I. J. Kang, C. H. Park, *Curr. Appl. Phys.* **2012**, *12*, S25.
[72] H. X. Deng, S. H. Wei, S. S. Li, J. Li, A. Walsh, *Phys. Rev. B – Condens. Matter Mater. Phys.* **2013**, *87*, 125203.
[73] S. Sallis, K. T. Butler, N. F. Quackenbush, D. S. Williams, M. Junda, D. A. Fischer, J. C. Woicik, N. J. Podraza, B. E. White, A. Walsh, L. F. J. Piper, *Appl. Phys. Lett.* **2014**, *104*, 232108.
[74] W. H. Han, Y. J. Oh, K. J. Chang, J. S. Park, *Phys. Rev. Appl.* **2015**, *3*, 44008.
[75] W. Körner, D. F. Urban, C. Elsässer, *Phys. Status Solidi A* **2015**, *212*, 1476.
[76] A. Walsh, J. L. F. Da Silva, S. H. Wei, *Chem. Mater.* **2009**, *21*, 5119.
[77] K. Nishio, T. Miyazaki, H. Nakamura, *Phys. Rev. Lett.* **2013**, *111*, 155502.
[78] P. P. Zawadzki, J. Perkins, S. Lany, *Phys. Rev. B* **2014**, *90*, 94203.
[79] K. Nomura, A. Takagi, T. Kamiya, H. Ohta, M. Hirano, H. Hosono, *Jpn. J. Appl. Phys.* **2006**, *45*, 4303.
[80] A. J. Leenheer, J. D. Perkins, M. F. A. M. Van Hest, J. J. Berry, R. P. O'Hayre, D. S. Ginley, *Phys. Rev. B* **2008**, *77*, 115215.
[81] T. Kamiya, K. Nomura, H. Hosono, *J. Disp. Technol.* **2009**, *5*, 273.
[82] T. Kamiya, K. Nomura, H. Hosono, *Appl. Phys. Lett.* **2010**, *96*, 122103.
[83] K. Makise, B. Shinozaki, T. Asano, K. Mitsuishi, K. Yano, K. Inoue, H. Nakamura, *J. Appl. Phys.* **2012**, *112*, 33716.
[84] D. B. Buchholz, Q. Ma, D. Alducin, A. Ponce, M. Jose-Yacaman, R. Khanal, J. E. Medvedeva, R. P. H. Chang, *Chem. Mater.* **2014**, *26*, 5401.
[85] S. Lee, D. C. Paine, *Appl. Phys. Lett.* **2013**, *102*, 52101.
[86] P. F. Ndione, A. Zakutayev, M. Kumar, C. E. Packard, J. J. Berry, J. D. Perkins, D. S. Ginley, *MRS Commun.* **2016**, *6*, 360.
[87] S. Sallis, N. F. Quackenbush, D. S. Williams, M. Senger, J. C. Woicik, B. E. White, L. F. J. Piper, *Phys. Status Solidi A* **2015**, *212*, 1471.
[88] H. Oh, S.-M. Yoon, M. K. Ryu, C.-S. Hwang, S. Yang, S.-H. K. Park, *Appl. Phys. Lett.* **2010**, *97*, 183502.
[89] A. L. Efros, B. I. Shklovskii, *Electronic Properties of Doped Semiconductors*, Springer-Verlag, Berlin, Heidelberg, **1984**.
[90] J. E. Medvedeva, in *Transparent Electron. From Synth. to Appl.* (Eds.: A. Facchetti, T. Marks), John Wiley & Sons, Hoboken, NJ, **2010**.
[91] K. Nomura, T. Kamiya, E. Ikenaga, H. Yanagi, K. Kobayashi, H. Hosono, *J. Appl. Phys.* **2011**, *109*, 73726.
[92] J. E. Medvedeva, R. Khanal, *Vacuum* **2015**, *114*, 142.
[93] R. Khanal, D. B. Buchholz, R. P. H. Chang, J. E. Medvedeva, *Phys. Rev. B* **2015**, *91*, 205203.
[94] N. F. Mott, E. A. Davis, *Electronic Processes in Non-Crystalline Materials*, Oxford University Press, Oxford, UK, **1971**.
[95] T. C. Yeh, Q. Zhu, D. B. Buchholz, A. B. Martinson, R. P. H. Chang, T. O. Mason, *Appl. Surf. Sci.* **2015**, *330*, 405.
[96] S. Lee, H. Park, Y. Do Kim, S. J. Tark, Y. Kang, W. M. Kim, H.-S. Lee, D. Kim, *Curr. Appl. Phys.* **2015**, *15*, 238.
[97] N. Zhou, D. B. Buchholz, G. Zhu, X. Yu, H. Lin, A. Facchetti, T. J. Marks, R. P. H. Chang, *Adv. Mater.* **2014**, *26*, 1098.
[98] C. Kittel, *Introduction to Solid State Physics*, John Wiley & Sons, Hoboken, NJ **2005**.
[99] P.-Y. Liao, T.-C. Chang, W.-C. Su, Y.-J. Chen, B.-W. Chen, T.-Y. Hsieh, C.-Y. Yang, Y.-Y. Huang, H.-M. Chang, S.-C. Chiang, *Appl. Phys. Express* **2016**, *9*, 124101.
[100] G. Kresse, J. Hafner, *Phys. Rev. B* **1993**, *47*, 558.
[101] G. Kresse, J. Hafner, *Phys. Rev. B* **1994**, *49*, 14251.
[102] G. Kresse, J. Furthmüller, *Comput. Mater. Sci.* **1996**, *6*, 15.
[103] G. Kresse, J. Furthmüller, *Phys. Rev. B* **1996**, *54*, 11169.
[104] J. P. Perdew, K. Burke, M. Ernzerhof, *Phys. Rev. Lett.* **1996**, *77*, 3865.
[105] P. E. Blöchl, *Phys. Rev. B* **1994**, *50*, 17953.
[106] G. Kresse, D. Joubert, *Phys. Rev. B* **1999**, *59*, 1758.
[107] R. Hoppe, *Angew. Chemie* **1970**, *82*, 7.
[108] R. Hoppe, S. Voigt, H. Glaum, J. Kissel, H. P. Müller, K. Bernet, *J. Less Common Met.* **1989**, *156*, 105.
[109] J. Heyd, G. E. Scuseria, M. Ernzerhof, *J. Chem. Phys.* **2003**, *118*, 8207.
[110] J. Heyd, J. E. Peralta, G. E. Scuseria, R. L. Martin, *J. Chem. Phys.* **2005**, *123*, 174101.
[111] K. Momma, F. Izumi, *IUCr, J. Appl. Crystallogr.* **2011**, *44*, 1272.

 © 2017 The Authors. Published by WILEY-VCH Verlag GmbH & Co. KGaA, Weinheim